Title
THE BREAKUP OF SPECTATOR RESIDUES IN RELATIVISTIC NUCLEAR COLLISIONS

Author
Warwick, A.I.

Publication Date
1982-10-01

LBL-14015
Preprint

Lawrence Berkeley Laboratory
UNIVERSITY OF CALIFORNIA

Submitted to Physical Review C

THE BREAKUP OF SPECTATOR RESIDUES IN RELATIVISTIC NUCLEAR COLLISIONS

A. I. Warwick, H. H. Wieman, H. H. Gutbrod, M. R. Maier, J. Péter, H. G. Ritter, H. Stelzer, F. Weik, M. Freedman, D. J. Henderson, S. B. Kaufman, E. P. Steinberg and B. D. Wilkins

October 1982

NUCLEAR SCIENCE DIVISION

Prepared for the U.S. Department of Energy under Contract DE-AC03-76SF00098

LBL-14015

The Breakup of Spectator Residues in Relativistic Nuclear Collisions

A.I. Warwick, H.H. Wieman, H.H. Gutbrod, M.R. Maier, J. Péter[a)],
H.G. Ritter, H. Stelzer, and F. Weik

Gesellschaft für Schwerionenforschung, D-1600 Darmstadt,
West Germany
and
Nuclear Science Division, Lawrence Berkeley Laboratory
University of California, Berkeley, CA 94720

M. Freedman, D.J. Henderson, S.B. Kaufman, E.P. Steinberg, and B.D. Wilkins

Chemistry Division, Argonne National Laboratory
Argonne, IL 60439

This work was supported in part by the Director, Office of Energy Research, Division of Nuclear Physics of the Office of High Energy and Nuclear Physics of the U.S. Department of Energy under Contracts DE-AC03-76SF00098 and W31-109-ENG-38.

ABSTRACT

Low energy nuclear fragments ($12 \leq A \leq 140$) from the bombardment of Au by high energy protons, ^{4}He, and ^{20}Ne projectiles are measured to yield information on the breakup of the target nucleus. We discuss the shapes of the fragment energy spectra across this broad range of fragment mass and pick out the fission component by its binary breakup. Multiplicities of coincident fast charged particles are presented as a measure of the degree of violence of the initial stage of the collision. Angular distributions of light fragments ($8 \leq Z \leq 11$) give the average velocities imparted to the residue in central collisions, and these values are compared to the results of cascade calculations. Measurements of slow fragment multiplicities from central events reveal a many-fragment final state. In the light of this finding we develop a simple calculation of the Coulomb features of the observed spectra. The applicability of a statistical breakup model is discussed.

NUCLEAR REACTIONS Au(^{20}Ne,HF) E = 5GeV, 8 GeV, 21 GeV, 42 GeV; Au(^{4}He,HF) E = 5 GeV; Au(p,HF) E = 4.9 GeV. Measured: $d^{2}\sigma/dEd\Omega$, associated multiplicites of fast charged particles, binary coincidences, slow fragment multiplicities.

I. INTRODUCTION

The study of high energy nuclear collisions has been pursued for many years, beginning with single particle inclusive measurements of target fragments from proton-nucleus collisions[1] and more recently turning to heavy ion collisions. In this recent work the emphasis has been on the hot regions of the interaction, where temperatures as high as 150 MeV have been observed[2] and where thermal models are quite successful[3]. In this paper we turn again to the breakup properties of the residue of a heavy target (Au) struck by a lighter projectile (p, ^{4}He, and ^{20}Ne), using one of the most comprehensive electronic detection system yet employed in such measurements.

The reaction mechanism is often divided into two steps, the first of which consists of a fast energy deposition stage during which fast light particles are emitted and the nuclear remnants are excited. This first stage can be treated, for example, as an intranuclear cascade[4] or more simply by a thermal fireball model[3]. In each case the decay of the excited spectator nuclear residue is considered as a slow second stage of the reaction. There is a temporal separation of the two stages and in the fireball model the fast and slow processes are separated spatially.

Deficiencies in the fireball results[2] raise questions about the clean-cut spatial separation of the nuclear matter into participant and spectator nucleons. The cascade approach describes a fast, initial stage of the collision that stops at a somewhat arbitrary cutoff point. Below a certain nucleon energy the cascading particles can not be correctly treated as classical colliding objects and are assumed to become part of the excited spectator residue. In this model the temporal separation of the two-step description is not entirely natural.

However, the decaying spectator residue produces slow fragments that exhibit spectra that are approximately independent of the mass and energy of the projectile. Any acceptable model must be able to describe this aspect of their production independently of the properties of the hot primary interaction region, which vary enormously with projectile energy.

In this paper we do not intend to put forward new models, rather we shall present aspects of our multi-parameter data and deduce properties of the fragment production mechanisms directly. We begin by surveying the fragment spectra across the broad range of masses observed. Measured fast charged particle multiplicities are presented and reveal the correlation between the violence of the initial collision and the mass of the fragments finally emitted. Angular distributions are presented and forward velocities are extracted for the source of fragments emitted in central collisions, using the two-step concept. We fall back to the cascade calculations to elucidate the discussion of these extracted velocities. Coincidence measurements of the slow fragments emitted from central collisions reveal a many-fragment breakup mechanism. Based on this finding we explore the equilibrium aspects of the breakup within the framework of a statistical model, and we develop a calculation of the Coulomb properties of the final state.

II. EXPERIMENTAL DETAILS

The data presented in this paper were obtained in the final version of a detector system that has served this group at the Bevalac for several years, becoming more complicated with each successive experiment and culminating in the version described here. Originally, very light reaction products and the associated multiplicities of fast charged particles were studied[5]. More recently the system has been devoted to measuring more massive fragments[6]. The latest version described here had a very general heavy fragment measurement capability and the theme of this experiment is to study the physics of target breakup across a wide range of product mass, charge, kinetic energy, and emission angle. The reactions studied lead in general to a many body final state and with this in mind the detectors provided a multi-coincidence capability, both among the slow fragments themselves and among these and the fast light charged particles that penetrate the vacuum chamber.

Figure 1 shows the chamber layout. The slow target fragment detectors were situated inside the thin-walled (3 mm) spherical aluminium vacuum chamber, the fast particles were measured outside the chamber. A variety of detection techniques were employed and the detector properties are discussed with regard to each of these techniques in the following sections.

A. Z-Identification Telescopes

Gas-silicon ΔE-E telescopes provided Z and energy measurement for light fragments[6]. These detector systems consisted of an ionisation chamber of CH_4 at a pressure of 30 Torr making a ΔE detector 20 cm deep. The detected fragments were stopped and their remaining energy measured in silicon surface barrier detectors 100 μ thick. Four gas volumes were in use, each containing three silicon E detectors, making 12 independent telescopes.

The four detector systems were centered at angles of -30°, +62°, +113°, and +151° with respect to the beam axis (we denote the left and right hemispheres of the chamber, looking downstream, by positive and negative angles, respectively). The most forward telescope was mounted such that the three Si detectors were in the horizontal plane, at angles of 125°, -30°, and 35°. The other telescopes were mounted with their Si detectors aligned vertically, with the central one in plane and the outer two at ±5° out of plane. Each Si detector subtended a solid angle of 2.9 msr. Depending on which of these silicons were allowed to trigger in singles mode (see Section F below) an angular distribution of up to six points could be obtained.

The pulse-height defect[7] of the silicon detectors was determined by measuring energy spectra of fission fragments from a ^{252}Cf source located at the position of the target, after removal of all intervening windows and gas so that the full energy of the fission fragment was deposited in the silicon detector. We found that a value of 12 for the parameter A of reference 7 was appropriate for all detectors.

The E and ΔE energy spectra were calibrated by comparing the signals produced by ^{252}Cf fission fragments with and without the presence of CH_4 gas in the ionisation chamber volume. This gave the slopes of the calibration. The offset was determined, in these and in all other heavy fragment spectra, by observing the position of the pedestal peak, caused by gating open the charge-sensitive ADC with no signal at the input and integrating the rectified noise. The pedestal peak thus represents the origin of the energy spectrum.

The identification was made, as in the previous work,[6] on the basis of a ΔE-E map. Having observed the position of the 6.1 MeV alpha particles from ^{252}Cf, the corresponding band was assigned as $Z = 2$ and the other visible bands numbered accordingly, up to $Z = 12$.

After Z identification, corrections were applied to the energy of the fragment for energy loss

a) in half the target thickness,

b) in the avalanche counter, for those two chambers viewing the target through the avalanche detector,

c) in the polypropylene window of the ionisation chamber, which had a thickness of 30 $\mu g\ cm^{-2}$,

d) in the dead layers of CH_4, 12 mm before the active ΔE volume and 12 mm between the ΔE volume and the silicon detector.

In cases a) and b) effective thicknesses were used that took into account the emission angle of the fragment. The source of dE/dx information was Northcliffe and Schilling[8] in each case and the maximum correction for fragments of Z = 12 amounted to 10% of the fragments' energy.

B. Avalanche Detectors

Two parallel plate avalanche detectors[9] were placed on either side of the target, 10 cm from the beam axis. These were very thin (equivalent to 150 $\mu g\ cm^{-2}$ of hydrocarbon), and fragments passed through to the TOF system described in section C) below. The thinness of these avalanche detectors provided a uniquely sensitive means of counting the presence or absence of heavy fragments emerging over a large solid angle between $\theta = 60^\circ$ and $\theta = 120^\circ$. The analogue signal from these detectors could be used with a software pulse-height threshold corresponding roughly to A = 30 so that when counting heavy fragments one could say with certainty that no alpha particles were contributing to the yield. With this off-line threshold the avalanche detectors were used in their own right to count binary breakup events exhibiting approximate two body kinematics in the laboratory frame.

Fragments detected by the ΔE-E telescopes at angles of 62° and 113° passed through the avalanche detector on that side of the target, thus allowing a determination of the detection efficiency of the avalanche detectors as a function of fragment charge and energy.

One electrode of each detector was segmented into vertical strips, 4 mm wide, read out through a resistive divider to provide position information along the horizontal coordinate. This and a fast timing signal were used as the start information for the time of flight system described in the next section.

The position calibration was performed by detecting fission fragments from ^{252}Cf passing through the avalanche detector into one of the silicons of the TOF system described below. The geometry of the ^{252}Cf source and of the silicon detector determined the mean horizontal coordinate of the point at which the fragment penetrated the avalanche detector so that by looking at avalanche position spectra in coincidence with different silicon detectors a calibration was achieved.

C. Time of Flight System

Two arrays of 100 μ thick silicon surface barrier detectors were arranged at $\theta \simeq 90°$ on either side of the beam, viewing the target through the thin avalanche detectors. These were the energy measuring stop detectors forming a TOF system with the avalanche counters as the start. One array consisted of three horizontal rows of four detectors, centered at angles of +80°, +85°, +90°, and +95°; the angles of the three rows with respect to the horizontal plane were -5°, 0°, and +5° (see Fig. 1). The opposite detector array spanned the angular range from -75° to -100° in 5° intervals, and the rows were at angles of 0°, 5°, and 10° with respect to the horizontal plane. Thus, correlation angles between coincident fragments could be measured over the range 155°-195°, and out-of-plane angles up to 15° were included.

The detectors were at a radius of 40 cm from the center of the chamber, resulting in a flight path of about 30 cm for the velocity measurement. Individual A resolution was not possible with such a short flight path; however, broad binning in A was required in any case because of the low counting statistics. The avalanche detectors became 100% efficient for fragments with A larger than about A = 15. Data from these silicon arrays are presented for $A \geq 20$. Punch through causes no problems for these heavier fragments and for $20 \geq A \gtrsim 50$ the acceptance includes all the yield; the spectra peak well above the low energy threshold. For heavier fragments the experimental low energy threshold cuts significantly into the yield and we observe only the high energy portion of the spectra.

The placing of the detectors around $\theta = 90^{\circ}$ on either side of the beam allows close examination of angular correlations between binary pairs of fragments and the study of perturbations of two body breakup kinematics.

The pulse-height defect and energy calibration were determined from ^{252}Cf fission fragment spectra in the same way as for the silicon detectors in the ΔE-E telescopes. The calibration of the TDCs, which were started by the avalanche detectors and stopped by the silicons, was achieved by observing the time spectra of the fission fragments and the 6.1 MeV alpha particles from ^{252}Cf.

After the mass of each fragment was determined, corrections to the measured energy were calculated due to

a) energy loss in the avalanche counter

b) energy loss in half the target thickness.

In both cases effective thicknesses were used depending on the fragment emission angle. The source of dE/dx information was Northcliffe and Schilling[8]. The maximum correction, for the slowest, heaviest fragments investigated, amounted to 20% of the energy of the fragment.

D. Target

The target was a self-supporting gold foil 500 $\mu g/cm^2$ thick, prepared by vacuum evaporation and mounted on a frame by means of several nylon filaments, ~10 μm thick, resulting in a nearly weightless support. It was placed at an angle of 15° to the beam, making it effectively thick in the beam direction, but thin for fragments emitted near 90°. This orientation preserved the sensitivity of the detectors but caused problems knowing how much of the beam missed the target. The target presented quite a small area to the beam (1 cm x 1 cm), which is notoriously unsteady at the Bevalac. The result is an uncertainty in the absolute normalisation of the double-differential cross sections presented here (see Section IIIA for estimates of this uncertainty).

E. Multiplicity Array

Outside the thin-walled (3 mm) spherical chamber the 80-fold paddle multiplicity array counted the number of fast charged particles emitted into most of the forward hemisphere in each event. This system has been described elsewhere[5,6] and was improved in this case by accumulating an ADC word for each scintillator. This allowed greater confidence in setting pulse-height thresholds off-line, above the background due to neutrons and gamma rays but below the smallest signals produced by charged particles, namely those from minimum ionising protons, which deposited 1 MeV in the scintillator paddles. Table 1 shows the minimum energy at which a given type of particle can penetrate the vacuum chamber to fire a scintillator.

F. Data Acquisition and Processing

The data acquisition system was made up of commercially available CAMAC hardware and will not be described in detail. However, a few words must be said about the triggering scheme, which is shown schematically in figure 2.

Each silicon detector, from the ion chamber telescopes or the TOF system, had the ability to trigger the CAMAC readout if an incident fragment deposited in it sufficient energy to produce a signal above the hardware threshold. The silicon detectors could be switched from singles to coincidence mode in any combination. All the detectors operated in coincidence mode all the time such that any pair of silicon detectors firing resulted in a coincidence event readout. However, only those detectors selected by the experimenter and switched to singles mode could cause a singles event readout, corresponding to an event with only one fragment detected. In addition, signals from the TOF system silicon detectors were required to have an accompanying avalanche signal (from either avalanche detector) before they were candidates to form an event trigger of any kind.

The experimenter could adjust the data rate for long-term beam intensity fluctuations by switching detectors into and out of 'selected singles'. Data could be taken with the emphasis on either fragment-fragment coincidences or on singles. Thus the data stream consisted of a mixture of singles, two-fold, and higher coincidences between any combination of fragment detectors. The proportion of coincidence to singles data depended on the number of silicon detectors switched into 'selected singles'. The multiplicity array was read out following each silicon detector trigger.

Data were accumulated with a dead time of approximately 50% and monitored by a pulser system, which sequentially pulsed the different groups of detectors during data taking, producing pulser events in the data stream for the purposes of gain stability checks, detector dead time and accidental background measurements.

The major data analysis program read the raw data tapes written by the on-line computer and produced output intermediate tapes of physical quantities

(fragment Z, A, energy, θ, ϕ, etc.) while preserving the event-by-event structure of the data stream. Smaller programs subsequently performed more particular analyses using the intermediate tapes as input; for example, one such program calculated single fragment inclusive cross sections.

III. DATA

In this section we have subdivided the data into self-contained topics, each showing one aspect of the measurements and presenting discussion of the points raised. We have arranged these topics in a pedagogical sequence so that discussion relies as far as possible on points that have already been made. We hope that in this way we can develop a broad view of the overall features of the reaction mechanisms as well as bringing out the details.

A. Single Fragment Inclusive Spectra

In the spirit of a survey of the features of the fragment spectra, across the full range of fragment mass, we present spectra from the TOF system in three mass bins $28 \leq A \leq 31$, $80 \leq A \leq 89$, and $120 \leq A \leq 139$. These data are summed over detectors situated at angles from $\theta = 75^\circ$ to $\theta = 100^\circ$, over which range no significant change in the spectra is observed.

Figure 3 shows these double differential cross sections from the bombardment of Au with 5 GeV Ne projectiles. The solid circles are the singles cross sections. The triangles represent the spectra of events satisfying a binary veto requirement that uses the large area avalanche detector on the opposite side of the target to the direction of emission of the measured fragment. Setting a software threshold on the pulse height of this opposite avalanche counter, corresponding approximately to a fragment mass of $A = 30$, the binary veto requirement is satisfied if there is no coincidence signal in the avalanche counter above this threshold. This vetoes events in which a coincident heavy fragment is emitted in the opposite direction and thus eliminates processes exhibiting approximate two-body kinematics in the laboratory frame. The spectra of light fragments typified by the mass bin $28 \leq A \leq 31$ in Fig. 31 show that only a small proportion of the fragments are thus vetoed and, furthermore, that there is no

particular part of the energy spectrum that is associated with such binary events. This can be interpreted as an indication that such light fragments are not formed to any significant extent in two-body processes.

In contrast, the spectra of medium-mass fragments (Fig. 3b) show the contribution of binary fission as a substantial fraction (~50%) of the fragments, removed by the binary veto in the energy range 50-80 MeV. This binary component is due to fission of target residues only a few mass units lighter than the target and moving slowly in the laboratory frame.[10]

The heavier fragments show only a small proportion of fission in the high-energy tail of the spectrum (Fig. 3c). The detailed arguments leading to the conclusion that the binary intermediate mass fragments are from conventional statistical fission are presented by us elsewhere[10,11] along with a method, based on measuring the number of fast charged particles emitted in the event, of separating the fission spectrum from that due to other mechanisms. The non-fission mechanism has been loosely termed 'deep-spallation' and we will bring out some of the features of this process in the discussions below.

For $\theta \simeq 90^\circ$ figure 4 shows the double differential cross sections for the lightest mass bin, $28 \leq A \leq 31$, for each of the six Au projectiles used. The Coulomb-like peak has been studied before[6,13] and falls within the energy acceptance of these detectors up to a fragment mass of $A \simeq 40$. Also shown on this figure are slope parameters (τ) from an exponential fit to the high energy tails of the curves. Figure 5 shows the 90° spectra for the intermediate mass bin $80 \leq A \leq 89$, which exhibit a fission fragment peak at about 60 MeV above the exponential tail of the deep-spallation spectrum. After separation by multiplicity[11] the fission fragment spectra are shown in figure 6 and the deep spallation spectra in figure 7. In the latter case

exponentials have been fitted to the spectra and the slope parameters (τ) are shown on the figure; they are considerably lower than was the case in the lightest mass bin. The data falling into the third mass bin $120 \leq A \leq 139$ are shown in figure 8. There is a small fission component in this mass region, but the spectra are essentially exponential, with small slope parameters as shown on the figure. The extracted slope parameters are discussed further in section G below.

Although the fragment double-differential cross sections are presented in mb sr^{-1} MeV^{-1} there is considerable uncertainty in the experimental absolute normalisation in some cases, due to the small target size and the large beam spots at the Bevalac. Table 2 gives the estimated systematic errors on $d^2\sigma/dEd\Omega$, which are constant for each bombardment. The error bars on the figures represent the statistical errors and are good for comparisons among data from a given bombardment, but not for cross comparisons between different bombardments.

B. Associated Fast Charged Particle Multiplicities

By means of techniques discussed previously[5] we have used the 80-fold array of scintillators (called paddles) to count the number of fast charged particles emitted in coincidence with the heavy fragments detected inside the vacuum chamber. The number of fast charged particles emitted is a direct measure of the violence of the initial collision. We use the term 'observed multiplicity' (m) to represent the number of scintillators hit in a single event. This quantity is detector dependent in as much as the array is made up of discrete elements covering only part of the solid angle. The experimental energy thresholds for the different particle types counted in the scintillators are shown in Table 1. We can study the observed multiplicity distribution P(m) associated with a variety of triggering fragments. The

detector dependence can be removed from the observed multiplicity distribution and the true differential mean multiplicity ($d\langle M\rangle/d\Omega$) can be calculated as a function of θ at three angles (15°, 33°, 63°) corresponding to the three paddle rings. Extrapolation and integration over 4π give the mean multiplicity $\langle M\rangle$. The necessary mathematics are presented elsewhere[5].

The aluminium mountings of the detectors inside the scattering chambers shadowed some of the 80 paddles, causing an effective increase in the detection thresholds over the values quoted in Table 1 and a consequent reduction in the yield. This was a small effect; the measured multiplicities were within 10% of those reported in reference 6, where the same paddle array was used with no shadowing inside the chamber.

Figure 9 shows the normalised observed multiplicity distributions associated with fragments of charge $6 \leq Z \leq 10$ detected at various angles, for two of the bombardments. This figure demonstrates the independence of the distributions on the angle at which the fragment is emitted, as has been observed previously for multiplicity distributions associated with lighter fragments[5].

Using this result we combine data associated with fragments from several of the TOF detectors situated around $\theta = 90°$. Figure 10 shows the observed multiplicity distributions P(m), normalised to unity, associated with fragments in each of the three mass bins $28 \leq A \leq 31$, $80 \leq A \leq 89$, $120 \leq A \leq 139$ for three bombardments, 4.9 GeV protons + Au, 5 GeV Ne + Au, and 42 GeV Ne + Au. Shown in figure 11, for 5 GeV Ne + Au, are contour plots of fragment yield versus fragment energy and associated observed multiplicity. The distributions P(m) are approximately symmetric curves except in the intermediate mass bin ($80 \leq A \leq 89$). In this case the contour plot shows two components due to deep spallation and fission[11], the latter contribution

causes the asymmetry on the low multiplicity side of the distribution P(m). Other than this fission contribution, the distributions show a smooth variation from high observed multiplicity associated with light fragments to lower observed multiplicity associated with heavy fragments. Figure 12 shows contours of fragment yield against fragment mass (A) and associated observed multiplicity (m), the fission yield is visible as a low multiplicity component at A ≅ 90, otherwise the trend is smooth. From this plot alone we can say that the heavy fragments ($A \gtrsim 120$) we observe are from a different class of events from those producing light fragments ($A \lesssim 20$) and the heavy fragments should not be regarded as residues left behind after the emission of the light fragments.

Figure 13 shows true mean multiplicities of fast charged particles <M> associated with fragments over the full mass range from several bombardments. For the 42 GeV Ne + Au, 21 GeV Ne + Au, and 8 GeV Ne + Au cases, all light fragments, up to A = 40, come from collisions of the same average degree of violence (same average fast particle multiplicity). At lower bombarding energies, 5 GeV Ne + Au, the fragments with A ≃ 30 have the highest associated multiplicity. Lighter fragments appear, on the average, to emerge from slightly less violent collisions.

For all four Ne bombardments shown in figure 13 the mean associated multiplicity dips to a minimum at the expected mass of fission fragments, due to the very low multiplicity fission component, rising again slightly as the trigger fragment mass becomes too large to be consistent with a fission mechanism. Using the fact that the fission component can be identified by the low associated observed multiplicity of fast charged particles (fig. 11b and reference 11), one can calculate mean multiplicities associated with only the deep spallation component. These are shown as open points on figure 13. The

result is a rather smooth trend of decreasing mean associated multiplicity of fast charged particles with increasing mass of the triggering fragment. At a fixed projectile energy, when one considers those events for which the violence of the initial stage of the collision and the fast particle multiplicity are greatest, the Au target residue is seen to break up most violently into the smallest pieces. One may consider the spallation process giving heavy fragments and the more violent breakup mechanism that gives light fragments simply as opposite ends of a spectrum of violence of the late-stage breakup, positively correlated with the violence of the initial fast stage of collisions induced by projectiles of a given energy.

The measured multiplicities of fast charged particles give an indirect experimental estimate of the mass number of the target spectator residue. The residue is defined to be that nuclear material left behind after the emission of the fast light particles from the hot region of primary interaction, and we estimate its mass number before it undergoes its inevitable breakup into slow nucleons and fragments. We make these estimates for central collisions in which there are few undetected leading particles. According to thermal models of the spectra[3], less than 20% of the yield of the fast charged particles lies undetected below the scintillator paddle thresholds shown in Table 1; this we neglect. We have converted the measured mean multiplicities of fast charged particles associated with the emission of a fragment of mass number A = 30 (central collisions) to the corresponding number of emitted nucleons, using the single particle inclusive cross sections for fast hydrogen and helium isotopes of reference 5 and the measured fast-neutron to fast-proton ratios of reference 12. Subtracting the resulting number of emitted fast nucleons from the mass number of the target-projectile system gives the estimated residue mass numbers of Table 3, shown for Ne + Au at four projectile energies.

Summarising the findings of section A and B, we find that the energy spectra of fragments of a given mass (A) are approximately independent of projectile energy, even though the violence of the initial fast stage of the collision (as measured by the fast particle multiplicity) increases dramatically with increasing projectile energy. On the other hand, at a given projectile energy, the more violent (high multiplicity) collisions lead, in the mean, to the production of lighter fragments than do the gentler, lower multiplicity collisions. Central collisions that at low bombarding energies just above the Coulomb barrier proceed through a fusion/fission or (HI,xn) channel are much more destructive at the high projectile energies studied here. At these energies only very gentle peripheral collisions can lead to fission, where the fissioning system is now the remnant of the Au target nucleus, analogous to Coulomb fission of the target at low energies.

C. Angular Distributions of Slow Light Fragments

In figure 14 we show, for each bombardment, double differential cross sections measured at four angles $\theta = 30^\circ, 62^\circ, 113^\circ, 151^\circ$, for $Z = 8$ fragments, which are typical of the light fragment region. It has become standard practice to extract the velocity of a moving, emitting source of fragments from such data as these. This has been done in the framework of the 'two-step vector model'[13], which in its simplest form involves the following assumptions.

a) There is a single moving source that emits fragments with equal probability in all directions in its rest frame.

b) The energy spectra of the emitted fragments are independent of the angle of emission in the rest frame of the source.

These assumptions are not entirely consistent with the measured data; references 6 and 13 contain discussion of the deficiencies of the model.

Because of the observed inconsistencies and the limited nature of our angular distribution measurement we have extracted source velocities in the simplest way, from the change in the energy at which the spectrum peaks in the laboratory frame as a function of angle θ. We have thus ignored the inconsistencies and regard the results as an estimate of the forward velocity transferred to the Au target residue during the initial stage of the collision. By measuring light fragments ($10 < A < 30$) we are observing rather violent central collisions, since these fragments have a high associated multiplicity of fast particles.

Table 4 shows the mean of the forward source velocities extracted from the spectra of fragments with $8 < Z < 11$ for each of the bombardments of Au studied. The velocity transferred during a central collision of Ne + Au decreases with increasing projectile energy in this domain of high projectile energy. For the proton and ^{4}He projectiles the transferred forward velocity is less than for Ne at the same total incident kinetic energy.

In order to obtain the energy integrated angular distributions of these fragments ($d\sigma/d\Omega$), the energy spectra of Fig. 14 must be extrapolated to both lower and higher energies. The high-energy extrapolation was done with an exponential function, and the low-energy one by means of a quadratic function going to zero cross section at zero energy. In no case was the correction for these extrapolations greater than 12%. The differential cross sections thus calculated are shown for the Ne projectiles in Fig. 15, normalized to unity for the 30° telescope for ease of comparison. The change in laboratory angular distribution from foward peaked at the two lower Ne energies to nearly isotropic at 42 GeV is clearly shown. The distributions for the proton and ^{4}He projectiles are intermediate between those for 8 GeV and 21 GeV Ne.

Similar changes in the angular distributions for light fragments with bombarding energy have been observed with protons.[14-17] Depending on the fragment studied, at proton energies above about 10 GeV a peak in the angular distribution at $\theta \simeq 60^\circ$-90° appears, and at 400 GeV the cross section is larger at backward angles than at forward angles.[16] It seems possible that such phenomena might be observed for Ne projectiles of higher energy than is now available.

D. Intra-Nuclear Cascade Calculations

The intranuclear cascade code of Yariv and Fraenkel[4] has been employed in an attempt to describe the initial stages of the observed nuclear collisions. These calculations describe the multiplicity of emitted fast nucleons very well. In particular, if one considers multiplicity distributions associated with a fast proton trigger particle emitted at 90°, the calculated charged particle multiplicity distributions are in good agreement with the data[4].

Here, however, we have measured mean multiplicities associated with the production of fragments. The results of cascade calculations support the idea that light fragments are produced in violent central collisions. The cascade calculations reproduce the measured multiplicities of fast charged particles associated with the detection of fragments in the mass range $10 \leq A \leq 30$ for calculated collisions in which the impact parameter is small.

Now consider the calculated properties of the target residue. The cascade excites the target nucleus by two processes.

a) Knocked out nucleons leave holes and the calculation of the corresponding excitation energies depends on the knowledge of the mean nucleon binding energy in the target nucleus. This process leads to a mean momentum transfer equal, in the first order, to the mean of the isotropically distributed Fermi momentum of the holes, which is zero. The inclusion in the calculation of energy dependent nucleon-nucleon cross sections and the treatment of the interaction of the knocked-out nucleon with the nuclear mean field by refraction at the field boundary introduce second order deviations from zero mean momentum transfer.

b) Slow cascade nucleons, which cannot be treated as classically cascading particles, are assumed to be absorbed by the residual target nuclear matter if their energy falls below a threshold[18]. In this way the target residue is excited and at the same time receives a finite mean momentum transfer in the direction of the beam.

Because of prohibitive computer costs we have not investigated the effects of varying the parameters of the cascade calculation. However, by considering points a) and b) above and by comparing measured and calculated values of the forward component of velocity transferred to the target residue during the initial collision we can draw some conclusions about the validity of the treatment of the residue excitation process in this particular cascade calculation.

We define the multiplicity of a calculated cascade event by counting the number of fast charged pions and protons above the experimental thresholds of Table 1. Noting that the contribution of He isotopes (and higher charges) to the measured multiplicity is rather small ($\lesssim$10%) we assume that the cascade multiplicity of charged pions and protons is equivalent to the measured multiplicity. This assumption has worked well in the past[4]. In figure 16a

we show contours of numbers of calculated events against multiplicity (M) and residue forward velocity ($\beta_{||}$). Figure 16b shows contours of numbers of calculated events against multiplicity (M) and target residue excitation. These plots are shown for those cases that are amenable to calculation by a cascade code, 5 GeV, 8 GeV, and 21 GeV Ne + Au. At higher energies the inelastic nucleon-nucleon processes are prohibitively complicated.

The arrows on the multiplicity axes indicate the measured values associated with fragments of $10 \leq A \leq 30$. By looking at the cascade events within a narrow window around these measured multiplicities we can extract the calculated mean forward residue velocities $\langle\beta_{||}\rangle$ and the calculated mean residue excitation energies of those cascade events that are expected to lead ultimately to emission of fragments of mass $10 \leq A \leq 30$. A similar procedure is adopted using the measured multiplicities associated with fission to extract the calculated forward velocities and excitations of the more peripheral cascade events expected to lead to fission. We have experimental values for $\beta_{||}$; for $10 \leq A \leq 30$ production these come from section C of this paper, for fission the experimental numbers are from reference 10, which is another report from this collaboration. These experimental values are compared with the cascade values extracted from figure 16 in table 4. In every case this particular cascade calculation underestimates the forward velocity transferred to the Au target residue, most noticeably at the lowest projectile energies. This is probably due to an underestimate, in the cascade calculation, of the effect of slowed, captured cascade particles, which are most important at the lowest energies. Such an underestimate implies that the calculated values of the residue excitation energy shown in table 4 are too small, particularly for the 5 GeV Ne + Au case. We regard these calculated values of the excitation energy as a rough lower limit.

E. Multiplicity of Target Fragments

We have presented some convincing pieces of evidence indicating that slow, light target fragments ($A \lesssim 40$) are produced in the more violent central collisions. In section A we showed single particle inclusive spectra for these light fragments. These spectra exhibit high energy tails with slopes of the order of 25 MeV, indicating a high excitation of the target residue. We also pointed out that at a given projectile energy the observed multiplicity of fast charged particles from the events that produce fragments is largest when the fragment mass is small ($\lesssim 40$). Thus the more violent initial stage of a central collision, during which a large number of measured fast charged particles are emitted, leads to a highly excited residue. Here we consider the possibility of a multiple breakup of the spectator matter in such central collisions.

In this section we examine events that lead to the production of a fragment of mass $20 \leq A \leq 40$ at $\theta = 90^\circ$, as a signature of the breakup of a highly excited target residue from a central collision. Mean multiplicities of slow, light fragments ($Z = 2$–27) emitted from the same event as the measured $A = 20$–40 fragment and detected inside the scattering chamber have been extracted from coincidence measurements.

Mean multiplicities of the associated fragments in the range $Z = 6$–27 were extracted from the slow fragment coincidence measurements using the following prescription. The differential mean multiplicity of fragment 2 associated with fragment 1 is given by the relation:

$$\frac{d\langle M(\chi_1,\chi_2)\rangle}{d\chi_2} = \frac{d\sigma_{12}(\chi_1,\chi_2)}{d\chi_1 d\chi_2} \quad \frac{d\sigma(\chi_2)}{d\chi_1}$$

where χ_i represents variables Ω_i (angle), E_i (energy), and Z_i or A_i (charge or mass, whichever is measured) for fragment i. In the reactions to

be considered here, particle 1 (the trigger particle with which particle 2 is associated) is detected in the TOF array at $\theta \simeq 90^\circ$ and has a mass between A = 20 and A = 40. Particle 2 is a fragment detected in an ion chamber telescope at $\theta = 30^\circ$, 62°, 113°, or 151° with a charge between Z = 6 and Z = 27. For these masses and charges 90% of the singles cross section lies within the kinetic energy acceptance of the detectors. The four point angular distribution for the coincidence measurements is shown in Fig. 17 for 5 GeV and 42 GeV Ne + Au. These distributions reflect the observed singles angular distributions, fairly isotropic for 42 GeV Ne + Au and forward peaked for 5 GeV Ne + Au. This lack of special angular correlation suggests that the reaction mechanism giving rise to the singles inclusive cross sections is also responsible for the coincidence events, i.e. it suggests that the coincidence requirement does not select out a different mechanism.

The mean multiplicity of associated slow fragments is found by extrapolating the four point angular distributions of Fig. 17 over 4π and depends on some assumptions about the out-of-plane dependence. Two different possible assumptions were tried:

a) a φ distribution symmetric about the beam and

b) symmetric about the direction of the mass 20-40 fragment detected at 90 degrees.

Both results agreed to within 12% with the result obtained by simply averaging the four points and multiplying by 4π. We have adopted this simple averaging in the analysis presented here.

In addition to measuring mean multiplicities of fragments with Z in the range 6 to 27 we have extended our analysis down to Z = 2, below the original design limits of the detector telescopes. This introduces uncertainties in individual Z identification due to small delta E signals and causes the loss

of higher energy fragments due to their punching through the silicon detectors. A comparison of our measured singles cross sections with Ne + U data[3] at 42 GeV shows agreement to within 5% for the summed cross sections from Z = 2 to 5. However, the large relative cross section for ^{4}He apparently contaminates our lithium identification leading to a factor of 3 error in the Z = 3 cross section.

In figure 18 the resulting mean multiplicities of the fragments associated with the A = 20–40 trigger particle are shown as a function of their charge. In the region Z = 6 and above, the error bars show only statistical uncertainties while in the region Z = 2 to 5 the error bars also include the uncertainties due to the Z misidentification mentioned above. The mean associated multiplicity increases rapidly with decreasing Z value to approximately 3 for He particles. For comparison the Z dependence of the singles cross section is also plotted. The Z dependence of the associated mean multiplicities and of the singles cross section are essentially the same, giving a second indication that the reactions sampled in these coincidence measurements are the same reactions giving rise to the inclusive cross sections.

The associated multiplicities are nearly the same for ^{4}He and ^{20}Ne projectiles with 5 GeV kinetic energy, somewhat smaller for 4.9 GeV proton projectiles. This is apparent in figure 19 where the associated multiplicities are summed from Z = 2 to Z = 27. There also appears to be only a small decrease as the neon projectile kinetic energy increases over the range from 5 to 42 GeV. Note that over this energy range the mean associated multiplicity of fast, light charged particles, measured in the 80-fold scintillator array, changes by a factor of 3 (an average of 13 fast charged particles are associated with a fragment of $20 \leq A \leq 40$ from the reaction

5 GeV Ne + Au, increasing to an average value of 42 associated with a fragment $20 \leq A \leq 40$ from the reaction 42 GeV Ne + Au). Apparently the slow fragment associated multiplicities do not depend strongly on the violence of the initial stage of the collision, measured by the fast particle multiplicities, as it changes with projectile energy.

F. Charge-Yield Curves

Having concluded that several slow fragments are present in the final state of a central collision of Ne + Au and having measured their mean multiplicities, we now compare the cross section for light fragment production, measured as a function of fragment charge, with the results of a statistical calculation of residue breakup. The calculation is by Fai and Randrup[19,20] and allows the excited residue to break up simultaneously into several pieces, weighting each possible exit channel by its final state phase space. Subsequent evaporation of the fragments is included. This model follows from earlier, less complete chemical equilibrium calculations.[3,21]

The model has two parameters, an effective volume (χ) and the available energy for nucleon in the residue (ϵ). $\chi = 1$ represents breakup over a volume equal to that of the residue at normal nuclear density and is used here. The results are somewhat dependent on the value of χ, see references 19 and 20. With a given value of χ the shape of the charge-yield curve depends strongly on the available energy in the system, which is varied to fit the experimental data.

Figure 20 shows the results. The open points are from reference 22 and are a measurement of hydrogen and helium yields at high emission velocities, extrapolated to include the yield of low energy particles. This extrapolation misses the large yield of alpha particles at a kinetic energy of about 20 MeV[3,13] and grossly underestimates the true yield; however, this

extrapolated high energy measurement can be regarded as the approximate contribution to the total yield from the primary interaction region, where the temperature is high. The dependence on Z of this contribution is fitted roughly by the calculation with available energy ε = 155 MeV per nucleon.

The solid triangles at Z = 2 and $6 \leq Z \leq 12$ are data from this experiment. Also shown is the yield of helium isotopes from the interaction of 42 GeV N + U.[3] In these cases the whole yield of alpha particles is included. We find a value of $\varepsilon \simeq 20$ MeV per nucleon to be appropriate to describe the charge-yield curve up to Z = 6.

The yields of fragments with $6 \leq Z \leq 12$ arise from central collisions, as indicated by the uniformly high associated multiplicity of fast charged particles shown in figure 13. We must be sure that most of the helium yield comes from this same class of events, otherwise fitting the Z = 2 and Z = 6 points of figure 20 with a single value of ε would be meaningless. Figure 18 shows that the singles charge-yield curve has the same shape as that obtained from central events triggered by the emission of a fragment of $A \simeq 30$. Thus one would infer that slow fragments from Z = 2 to $Z \simeq 12$ are produced for the most part in the same class of events. This implies that a sucessful statistical breakup calculation should fit the shape of the entire range of data in figure 20 with a common value of ε. To our knowledge the model cannot reproduce the measured shape above Z = 6. This may be due to the breakdown of statistical assumptions or the onset of nonequilibrium behaviour.

We can discuss the temperature of relative motion of the fragments if we note that such a quantity represents an average over many finite events. Such an averaging procedure is equivalent to increasing the size of a single event to reach the thermodynamic limit and it is in this sense that we speak of temperature.[19] The calculation of Fai and Randrup with $\chi = 1$ and ε = 20 MeV

produces fragments with a mean mass number A = 2.4 and after energy is taken up to break the binding the temperature of the relative motion of the fragments is T = 24 MeV. This quantity is experimentally accessible and is discussed further in section G.

G. Coulomb Features of the Spectra

In figure 21 are shown the spectra of fragments of different Z values for the reaction 5 GeV Ne + Au. In figure 14 are the angular distributions of the fragments of Z = 8 from each of the reactions. These figures, together with spectra of figure 4, illustrate the behavior of the peak in the light fragment spectra and the evidence for its association with the Coulomb potential of an emitting system.

a) The peak moves to higher energies as the Z of the fragment increases (fig. 21) as would be the case if the fragment were emitted in the Coulomb field of a larger system.

b) The peaks move to lower energies and become slightly broader as the energy of the projectile is increased (fig. 4). The initial stages of the collisions are more violent at the higher bombarding energies and the mass and charge of the residual system from which the light fragment is emitted are thus smaller, giving a lower Coulomb energy. The peak is broader because the more violent initial stage leaves residues with a broader range of excitation, motion, and size.

c) A conventional picture is one in which the Coulomb barrier against light fragment emission can be calculated after reckoning the residue size by measuring the mass removed from the target during the initial stage of the collision (fast particle multiplicity) and allowing this residue to split into two touching spheres, one of which is the fragment to be detected, the other becomes a massive slowly moving residue. Such a calculation gives a Coulomb barrier too large to explain the data by approximately a factor of two[6,13].

In section E we presented the measured mean multiplicities of light slow fragments ($Z \leq 27$) emitted in coincidence with a trigger fragment of mass number between 20 and 40. These results indicate that the collisions that lead to the emission of $20 \leq A \leq 40$ fragments typically involve several slow light fragments in the final state. Furthermore, in the case of 42 GeV Ne + Au, the number of nucleons represented by the slow fragment multiplicity and by the multiplicity of fast charged particles, together with an estimate of the unobserved neutrons, is large enough to account for the complete mass of the target and projectile system. Table 5 shows the mass balance for 5 GeV and 42 GeV Ne + Au. The fast charged particle multiplicities are converted approximately to numbers of nucleons using the single particle inclusive cross sections for hydrogen and helium isotopes from reference 5 and including an estimate for the unobserved fast neutrons, in the same way as in section B. The slow fragment multiplicities of figure 18 give an estimate of the number of nucleons represented by assuming that these fragments have mass numbers equal to twice the measured value. The number of slow protons (not fast enough to penetrate the vacuum chamber and hence not counted in the scintillator array) are obtained by extrapolating the results shown in figure 19 to $Z = 1$, based on the cross sections measured for slow, low-Z fragments by Poskanzer et al.[13] Reference 12 provides measured neutron/proton ratios, which are subsequently used to estimate the numbers of slow neutrons.

Table 5 shows that there is a considerable unobserved mass at 5 GeV but that in collisions leading to the emission of fragments of $A \simeq 30$ at 42 GeV, the trigger fragment, the fast particles, and the slow charged particles and neutrons account for almost the entire mass of the target-projectile combination. At this high energy there is no unobserved heavy residue in these collisions.

Based on this observation we develop the following calculation of the Coulomb properties of the final state, with a view to calculating the observed fragment energy spectra at 90° and learning the relationship between the slope of the observed sectra (τ) and the temperature of the relative motion of the fragments immediately following the breakup.

In the case of 42 GeV Ne + Au, the forward momentum transferred to the nuclear residue during the initial stage of the collision is small ($<\beta_{\parallel}> \simeq$ 0.006, section C). The light fragment energy spectrum ($28 \leq A \leq 31$, fig. 4) is measured at 90° in the lab and would, to a good approximation, be unchanged by a transformation to a frame of reference moving forward with this mean velocity. We will calculate the Coulomb properties of the final state in this slowly moving frame and compare the results to the spectra measured at 90° in the laboratory for the 42 GeV Ne + Au case.

The mass balance of Table 5 shows that after the initial emission of fast charged particles and after the slow neutrons are accounted for, there remains a system of $Z \simeq 41$, which breaks up into the light slow charged fragments.

Using a Monte Carlo technique we generate the late stage of an event consisting of a variable number of fragments of varying charge, one of which is constrained to have $Z = 15$, $A = 30$ since we wish to compare the results to the measured spectra from events triggered by the detection of such a fragment ($28 \leq A \leq 31$ at $\theta = 90°$). The Z distribution of the remaining fragments is constrained to follow the shape of the measured multiplicity distribution of slow charged fragments shown, for 42 GeV Ne + Au, in figure 18. Fragments are picked from the distributions and assigned velocities such that they all satisfy a Maxwell-Boltzmann kinetic energy distribution with temperature T, until the summed charge of the fragments reaches 41 and represents the entire charge of the residue. For simplicity the fragments are arranged randomly in

space on the corners of a cubic lattice and the initial density of fragments (ρ), along with the temperature (T), are regarded as variable parameters. The fragments are allowed to move apart on classical trajectories under the influence of the Coulomb field and the asymptotic kinetic energies are histogrammed. The calculation is repeated for 5000 events. We have ignored the possibility of shape distortion of the residue, caused for example by hydrodynamic flow, and the possible effects on such a Coulomb calculation as this.

The idea is that the calculation should begin after the late-stage breakup, when the fragments are no longer in nuclear contact. Under these circumstances the system is classical and nonrelativistic, and Maxwell-Boltzmann statistics are appropriate. The Coulomb force is considered explicitly only after the breakup process is complete. The sizes of the fragments are prescribed by the data, and we wish to determine the initial temperature that corresponds to the observed value of τ.

The average Monte Carlo event has 13 charged fragments in the range $1 \leq Z \leq 30$ and a total momentum in the calculation frame of $\simeq$2 GeV/c, oriented randomly. The ensemble of many such events is statistically equivalent to a single thermodynamic ensemble[19] and it is in this sense that we speak of temperature.

Figure 22 shows the results and the 42 GeV Ne + Au data. The best fit is obtained with an initial temperature T = 20 MeV and initial density one fifth that of nuclear matter, 5×10^{-3} charged fragments fm^{-3}, corresponding to fragments initially 5.8 fm apart. Calculations beginning earlier than this, at lower temperatures (e.g. 15 MeV) and higher densities (e.g. 1×10^{-2} charged fragments fm^{-3}) give poorer fits. This is interpreted as meaning that at these higher densities the internal nuclear degrees of freedom of the fragments are still important. (These are ignored in the calculation.)

As the expansion progresses, all fragments experience an increase in their apparent temperatures (τ). Alpha particles change from T = 20 MeV to an asymptotic value of τ = 26 MeV, the A = 30 fragments change from T = 20 MeV to τ = 34 MeV. The peak of the initial Maxwell-Boltzmann distribution broadens and moves to higher energies. Although the final temperature calculated for the A = 30 fragments is somewhat larger than that of the data we conclude that a temperature of T ≃ 20 MeV is appropriate to describe the average relative motion of the fragments immediately after they are formed.

The extracted value of T ≃ 20 MeV should be compared with the final ensemble temperature of T = 24 MeV produced by the statistical breakup calculation of Fai and Randrup at an excitation of 20 MeV per nucleon. We regard these values as encouragingly consistent, indicating that an excitation around 20 MeV per nucleon is appropriate for the spectator residues in central collisions of 42 GeV Ne + Au. Furthermore, the close similarity of the fragment spectra as the projectile energy is changed suggests that this 20 MeV breakup excitation is rather universal.

When the energy of the Ne projectile is reduced to 5 GeV the Z dependence of the slow charged particle multiplicity from central collisions, shown in figure 19, changes slightly. These coincidence measurements show relatively more yield at higher Z values (figure 18) and the integrated slow fragment multiplicity is about 20% higher than at 42 GeV (figure 19). The measured mean size of the residue, shown in table 3, is significantly larger at this lower energy, A ≃ 170 instead of A ≃ 110 with 42 GeV Ne. The increased slow fragment multiplicities reflect this increased residue size but cannot account for all of it. The reaction mechanism must be such as to heat only part of the larger residue to the breakup excitation leaving a region of lower excitation to form slowly moving heavy fragments, which are undetected in this experiment.

Whatever the details of the mechanism, the multi-fragmentation of the residue of central collisions is likely to proceed rapidly. The concept of a two-step reaction, which has been so useful in analyzing these collisions, seems still to be valid, even though the time scales of the initial cascade and the residue breakup may be comparable. This is demonstrated graphically by the angular distributions of the fast charged particles emitted from the cascade and of the slow charged particles from the residue breakup. The former are strongly forward peaked; the latter are almost isotropic in the laboratory frame at the highest projectile energy measured here (42 GeV Ne).

IV. CONCLUSION

We have studied several features of the collisions of relativistic projectiles with a heavy target, using a broad experimental approach. The resulting data are not simply a large body of cross sections but a necessarily complicated mixture of different kinds of results. We have presented and interpreted them, as far as possible, in a model independent way.

Fission is always present in these collisions and can be understood as a peripheral process; conventional ideas are not challenged. Similarly, the peripheral collisions leading to heavy residues with low excitation seem to fit with a conventional evaporation scenario. However, the central collisions leading to the multi-fragmentation of a highly excited residue are not part of the conventional picture. The integrity of models of the residue breakup mechanisms in these central collisions is yet to be firmly established; however, a treatment that allows for fast, unrelaxed disintegration seems to be appropriate, with a characteristic excitation energy of 20 MeV per nucleon.

ACKNOWLEDGMENTS

We acknowledge the support and encouragement of A.M. Poskanzer and useful discussions with G. Fai, J. Randrup, J. Harris, and R. Stock. Credit is due to W.G. Meyer, who helped conceive the experiment, and to C. Riedel, who performed the intranuclear cascade calculations. This work was supported in part by the Director, Office of Energy Research, Division of Nuclear Physics of the Office of High Energy and Nuclear Physics of the U.S. Department of Energy under Contracts DE-AC03-76SF00098 and W31-109-ENG-38.

Table 1

Thresholds for Charged Particles Detected

in the 80-fold Scintillator Array

Particle	Energies
π^+	10 MeV
p	25 MeV
d	17 MeV per nucleon
t	13 MeV per nucleon
^{3}He	29 MeV per nucleon
^{4}He	25 MeV per nucleon

Table 2

Uncertainties in Absolute Normalisation

of the Fragment Cross Sections

Reaction	Systematic Uncertainty
4.9 GeV p + Au	30%
1.25 GeV/u ^{4}He + Au	30%
250 MeV/u ^{20}Ne + Au	50%
400 MeV/u ^{20}Ne + Au	30%
1.05 GeV/u ^{20}Ne + Au	30%
2.1 GeV/u ^{20}Ne + Au	50%

Table 3

Experimental Estimates of Spectator Residue Mass Numbers

in Events Leading to the Emission of A = 30 Fragments

$$A_R = A_{proj} + A_{tgt} - \langle M \rangle_{fast\ nucleons}$$

Reaction	Estimated Residue Mass (A_R)
5 GeV Ne + Au	170
8 GeV Ne + Au	160
21 GeV Ne + Au	140
42 GeV Ne + Au	110

Table 4

Forward Velocities and Excitation Energies of the Au Target Residue

Reaction	Trigger Fragment	Mean Measured Multiplicity <M>	Mean Measured Forward Velocity $<\beta_{\parallel}>$	Cascade Calculated $<\beta_{\parallel}>$	Cascade Calculated Excitation Energy <E*> (GeV)	Cascade Calculated Residue Mass Number <A>
4.9 GeV	light[a]		0.006 ± 0.002	not	not	not
p + Au	fission[b]		0.0015 ± 0.0003	calculated	calculated	calculated
5 GeV	light	12	0.009 ± 0.002	0.002	0.6	176
He + Au	fission	3	0.0012 ± 0.0003	0.006	0.2	
5 GeV	light	12	0.018 ± 0.001	0.007	0.8	178
Ne + Au	fission	3	0.0036 ± 0.0004	0.001	0.14	
8 GeV	light	19	0.014 ± 0.003	0.0075	1.0	165
Ne + Au	fission	3	0.0030 ± 0.0003	0.0007	0.13	
21 GeV	light	28	0.009 ± 0.002	0.0055	1.2	141
Ne + Au	fission	5	0.0009 ± 0.0002	0.0003	0.15	
42 GeV/u	light		0.006 ± 0.002	not	not	not
Ne + Au	fission		0.0009 ± 0.0002	calculated	calculated	calculated

a) The light fragments are from central collisions. Mean measured multiplicities <M>, used to extract $<\beta_{\parallel}>$, <E*>, and <A> from cascade calculations, are associated with a fragment of mass $10 \leq A \leq 30$. The experimental values of $<\beta_{\parallel}>$ are extracted from spectra of fragments in the range $8 \leq \overline{Z} \leq \overline{11}$.

b) Fission occurs in the most peripheral collisions. Fission events give $<\beta_{\parallel}>$ via the two-body breakup kinematics[10] and the associated multiplicities are used to extract corresponding values of $<\beta_{\parallel}>$ and <E*> from the cascade calculations.

Table 5

Mass balance for Ne + Au collisions leading to the Emission of a Fragment of A = 20-40

	5 GeV Ne + Au		42 GeV Ne + Au	
Product	Mean Multiplicity	Approximate Number of Nucleons	Mean Multiplicity	Approximate Number of Nucleons
Trigger fragment	1	30	1	30
Fast charged particles	13	17	42	50
Fast Neutrons	29	29	60	60
Slow charged fragments (Z = 2-27)	6	45	5.6	39
Slow protons	6	6	6	6
Slow Neutrons	24	24	24	24
		Total = 135		Total = 209

References

a) Present address: IPN 91406 Orsay, France

1. I. Dostrovsky, R. Davis, A.M. Poskanzer, and P.L. Reeder, Phys. Rev. 139 (1965) 1513 and references therein
2. H.H. Gutbrod, A.I. Warwick, and H.H. Wieman, Nucl. Phys. A387 (1982)
3. J. Gosset, H.H. Gutbrod, W.G. Meyer, A.M. Poskanzer, A. Sandoval, R. Stock, and G.D. Westfall, Phys. Rev. C16 (1977) 629
4. Y. Yariv and Z. Fraenkel, Phys. Rev. C20 (1979) 2227
5. A. Sandoval, H.H. Gutbrod, W.G. Meyer, R. Stock, C. Lukner, A.M. Poskanzer, J. Gosset, J.C. Jourdain, C.H. King, G. King, N. Van Sen, G.D. Westfall, and K.L. Wolf, Phys. Rev. C21 (1980) 1321
6. W.G. Meyer, H.H. Gutbrod, C. Lukner, and A. Sandoval, Phys. Rev. C22 (1980) 179
7. S.B. Kaufman, E.P. Steinberg, B.D. Wilkins, J. Unik, A.J. Gorski, and M.J. Fluss, Nucl. Instr. Meth. 115 (1974) 47
8. L.C. Northcliffe and R.F. Schilling, Nucl. Data Tables A7 (1970) 233
9. H. Stelzer and A. Baden, Nucl. Science Div. Ann. Rep. (1979-80), Lawrence Berkeley Lab., Univ. of Calif.
10. S.B. Kaufman, et al., Phys. Rev. C to be published
11. A.I. Warwick, et al., Phys. Rev. Lett. 48 (1982) 1719
12. W. Schimmerling, J.W. Kast, D.O. Dahl, R. Madey, R.A. Cecil, B.D. Anderson, and H.R. Baldwin, Phys. Rev. Lett. 43 (1979) 1985
13. A.M. Poskanzer, G.W. Butler, and E.K. Hyde, Phys. Rev. C3 (1971) 882
14. L.P. Remsberg and D.G. Perry, Phys. Rev. Lett. 35 (1975) 361

15. D.R. Fortney and N.T. Porile, Phys. Lett. 76B (1978) 553; Phys. Rev. C21 (1980) 2511

16. N.T. Porile, et al., Phys. Rev. Lett. 43 (1979) 918

17. J.A. Urbon, S.B. Kaufman, D.J. Henderson, and E.P. Steinberg, Phys. Rev. C21 (1980) 1048

18. K. Chen, Z. Fraenkel, G. Friedlander, J.R. Grover, J.M. Miller, and Y. Shimamoto, Phys. Rev. 166 (1968) 949

19. J. Randrup and S.E. Koonin, Nucl. Phys. A356 (1981) 223

20. G. Fai and J. Randrup, Nucl. Phys. A381 (1982) 557

21. A. Mekjian, Phys. Rev. Lett. 38 (1977) 640; Phys. Rev. C17 (1978) 1051

22. S. Nagamiya, et al., Phys. Rev. C24 (1981) 971

Figure Captions

Fig. 1. Layout of the scattering chamber.

Fig. 2. Schematic diagram of trigger logic.

Fig. 3. Double differential cross sections for fragments falling into three mass bins a) $28 \leq A \leq 31$, b) $80 \leq A \leq 89$, and c) $120 \leq A \leq 129$. The solid circles are the unselected cross sections, the open triangles are from events satisfying the binary veto requirement described in the text.

Fig. 4. Double differential cross sections for fragments falling into the lightest mass bin, for each of the reactions studied. The exponential slope parameters (τ) are from a fit to the tails of the spectra.

Fig. 5. Double differential cross sections for fragments falling into the intermediate mass bin, for each of the reactions studied.

Fig. 6. Double differential cross sections for fission fragments extracted from the intermediate mass bin by the multiplicity technique of reference 11, for each of the reactions studied.

Fig. 7. Double differential cross sections for deep spallation products extracted from the intermediate mass bin by the technique of reference 11, for each of the reactions studied. The exponential slope parameters (τ) are from a fit to the tails of the spectra.

Fig. 8. Double differential cross sections for fragments falling into the heaviest mass bin, for each of the reactions studied. The exponential slope parameters (τ) are from a fit to the tails of the measured spectra.

Fig. 9. Fast charged particle observed multiplicity distributions associated with fragments of $6 \leq Z \leq 10$ measured at various angles. The distributions are independent of the angle of emission of the trigger fragment.

Fig. 10. Fast charged particle observed multiplicity distributions associated with fragments at $\theta \approx 90^\circ$ in each of the mass bins a) $28 \leq A \leq 31$, b) $80 \leq A \leq 89$, and c) $120 \leq A \leq 129$, for three of the reactions studied.

Fig. 11. Contours of fragment yield against associated observed multiplicity and fragment energy, for the reaction 5 GeV Ne + Au producing fragments in the three mass bins a) $28 \leq A \leq 31$, b) $80 \leq A \leq 89$, and c) $120 \leq A \leq 129$.

Fig. 12. Contours of fragment yield against associated observed multiplicity and fragment mass for the reaction 42 GeV Ne + Au.

Fig. 13. Measured mean multiplicities of fast charged particles associated with fragments of mass A, as a function of A, for each of the Ne bombardments studied. The open points are multiplicities associated with nonfission events.

Fig. 14. Angular variation of the spectra of fragments of $Z = 8$ from the reactions a) 4.9 GeV p + Au, b) 5 GeV He + Au, c) 5 GeV Ne + Au, d) 8 GeV Ne + Au, 3) 21 GeV Ne + Au, and f) 42 GeV Ne + Au.

Fig. 15. Angular distribution of $Z = 8$ fragments from the reaction Ne + Au at the four projectile energies studied.

Fig. 16. Results of the cascade calculation of Yariv and Fraenkel for the interaction Ne + Au at three of the measured projectile energies. The plots show contours of numbers of calculated events a) against multiplicity and target residue forward velocity (in units of v/c) and b) against multiplicity and target residue excitation energy (GeV). The arrows on the multiplicity axes indicate the measured multiplicities associated with fragments of mass A = 30, the arrows on the abscissae show the corresponding calculated values of $\beta_{||}$ and excitation energy.

Fig. 17. Differential mean multiplicities of fragments with $6 \leq Z \leq 27$ associated with a trigger fragment of mass A = 20–40 detected at $\theta_1 \simeq 90^\circ$ from the reaction of Ne + Au.

Fig. 18. Open circles show the mean multiplicities of fragments with charge Z associated with a trigger fragment of mass A = 20–40 detected at $\theta \simeq 90^\circ$ from the reaction Ne + Au. The histogram represents the singles measurement of fragment yield as a function of fragment charge Z, scaled arbitrarily for comparison to the measured fragment multiplicities.

Fig. 19. Mean multiplicity of slow fragments with Z in the range $2 \leq Z \leq 27$ associated with a trigger fragment of mass $20 \leq A \leq 40$ detected at $\theta \simeq 90^\circ$. The mean multiplicity is shown for three projectiles (p, He, Ne) at 5 GeV kinetic energy and for Ne projectiles at four energies 5 GeV, 8 GeV, 21 GeV, and 42 GeV.

Fig. 20. Cross sections for fragment production from the interaction of 42 GeV Ne with heavy targets as a function of fragment charge (Z). The statistical calculations of Fai and Randrup are normalised so that the ϵ = 20 MeV curve passes through the Ne + Au data points.

Fig. 21. Double differential cross sections of fragments of various Z values measured at $\theta = 62^{\circ}$ from the reaction 5 GeV Ne + Au.

Fig. 22. Results of the Coulomb expansion calculation of the kinetic energy spectra of A = 30 fragments emerging from the Au target residue after a central collision induced by a 42 GeV Ne projectile.

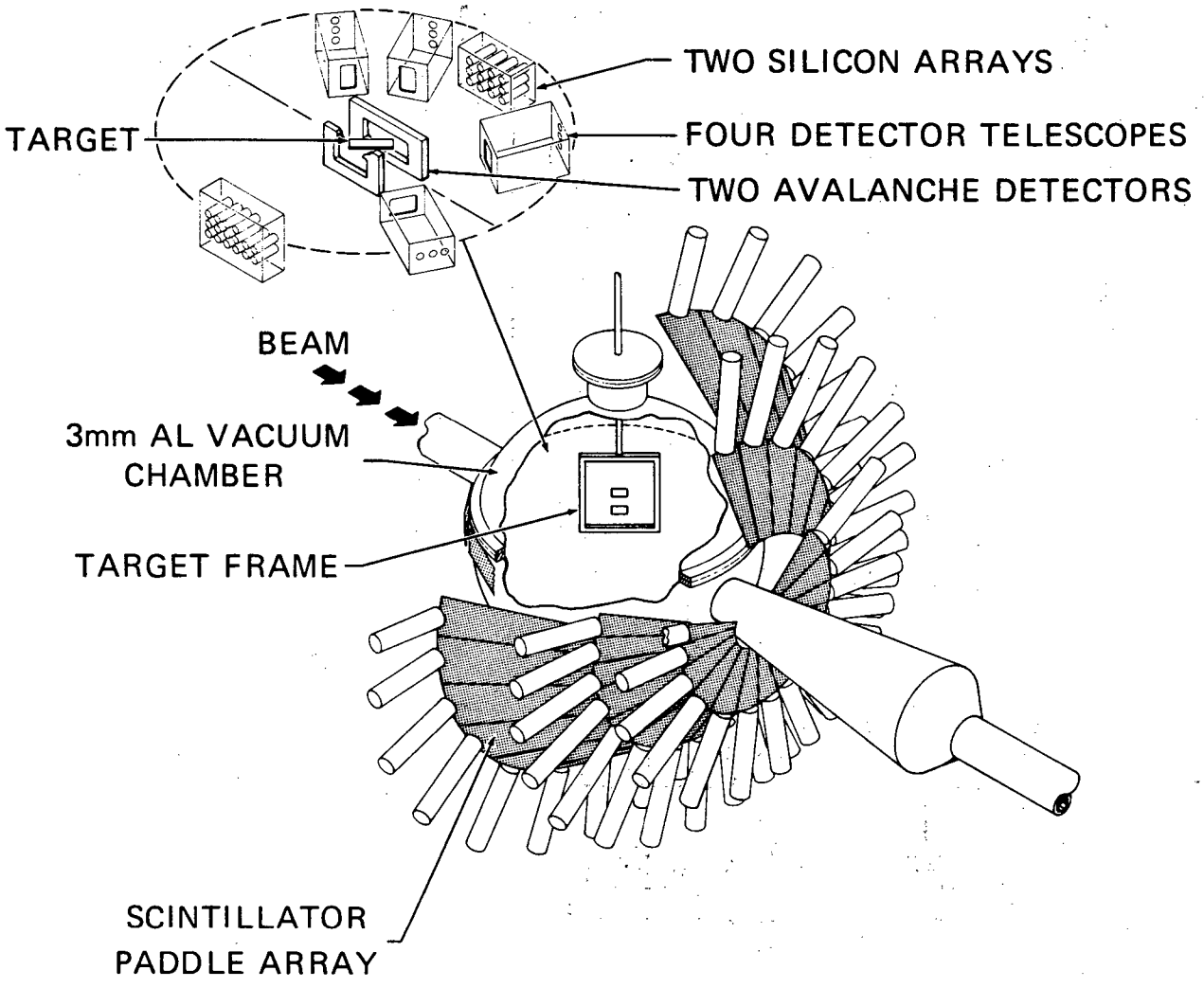

Fig. 1

XBL 808-1691A

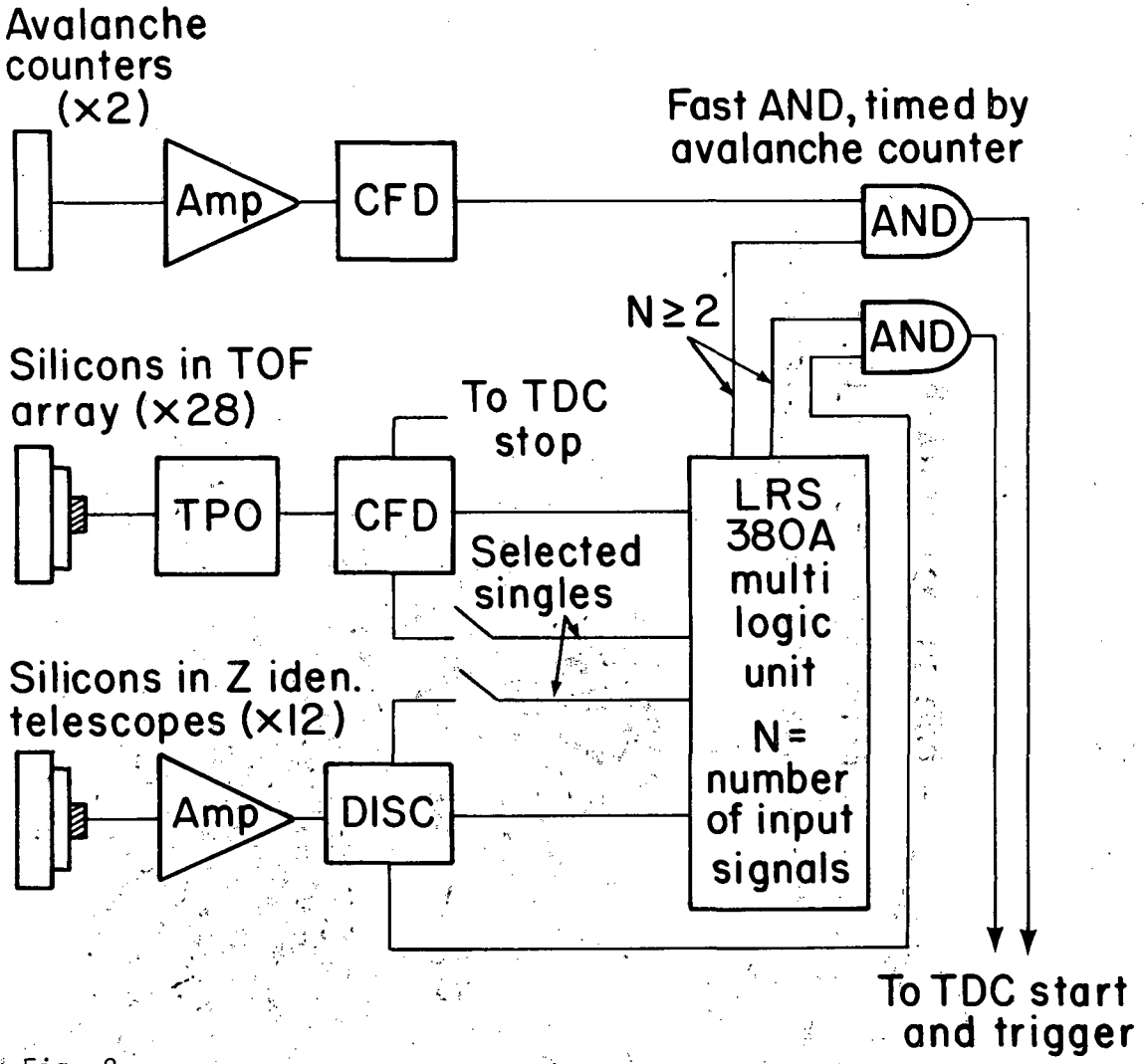

Fig. 2

XBL 822-144

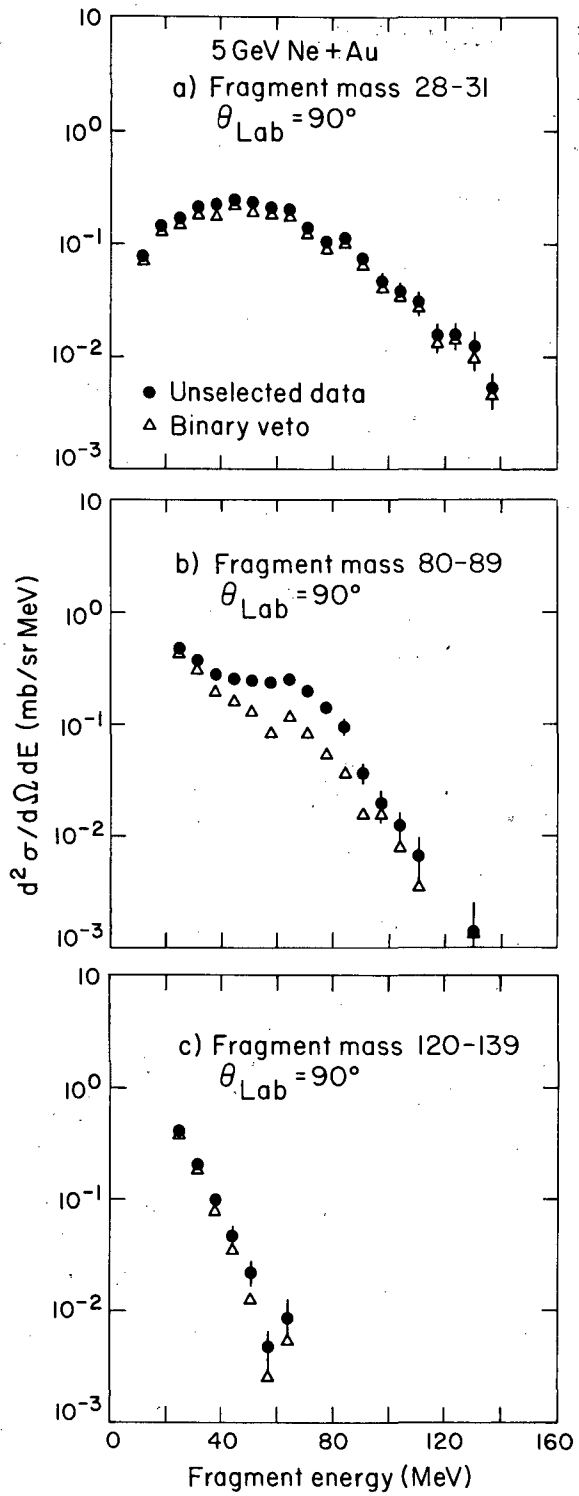

Fig. 3

XBL 827 – 893

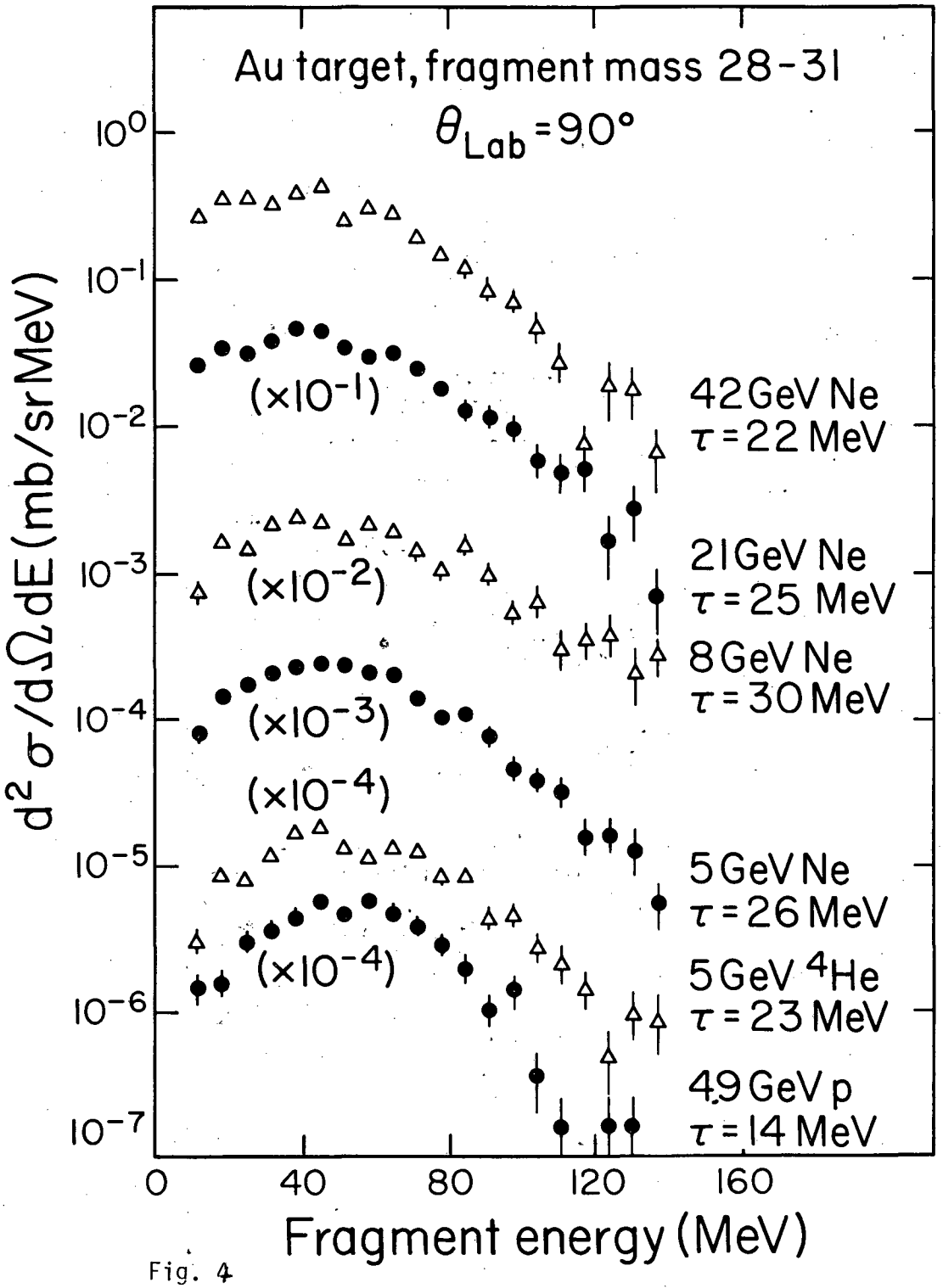

Fig. 4

XBL 8112-1652

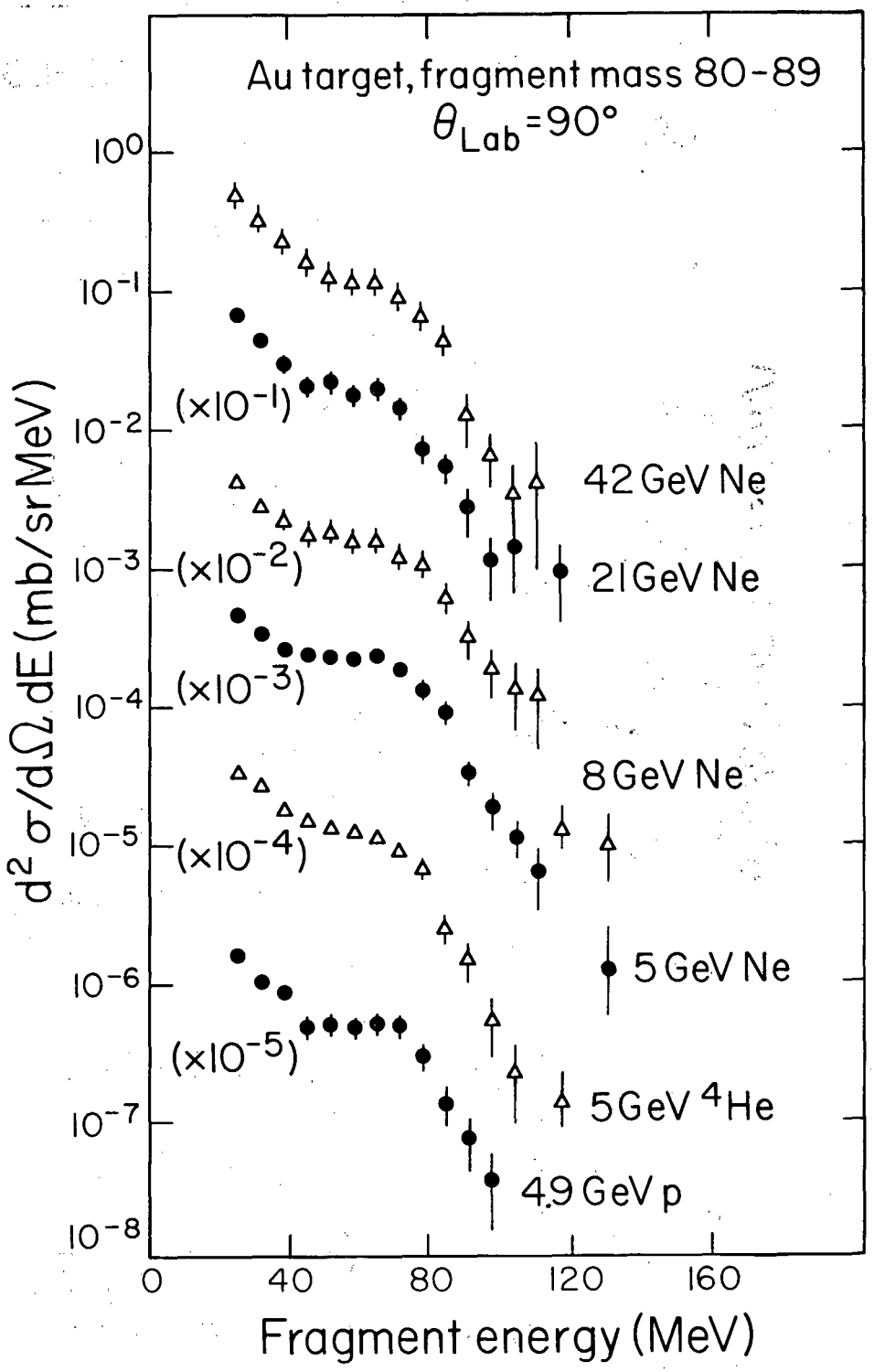

Fig. 5

XBL 823-245

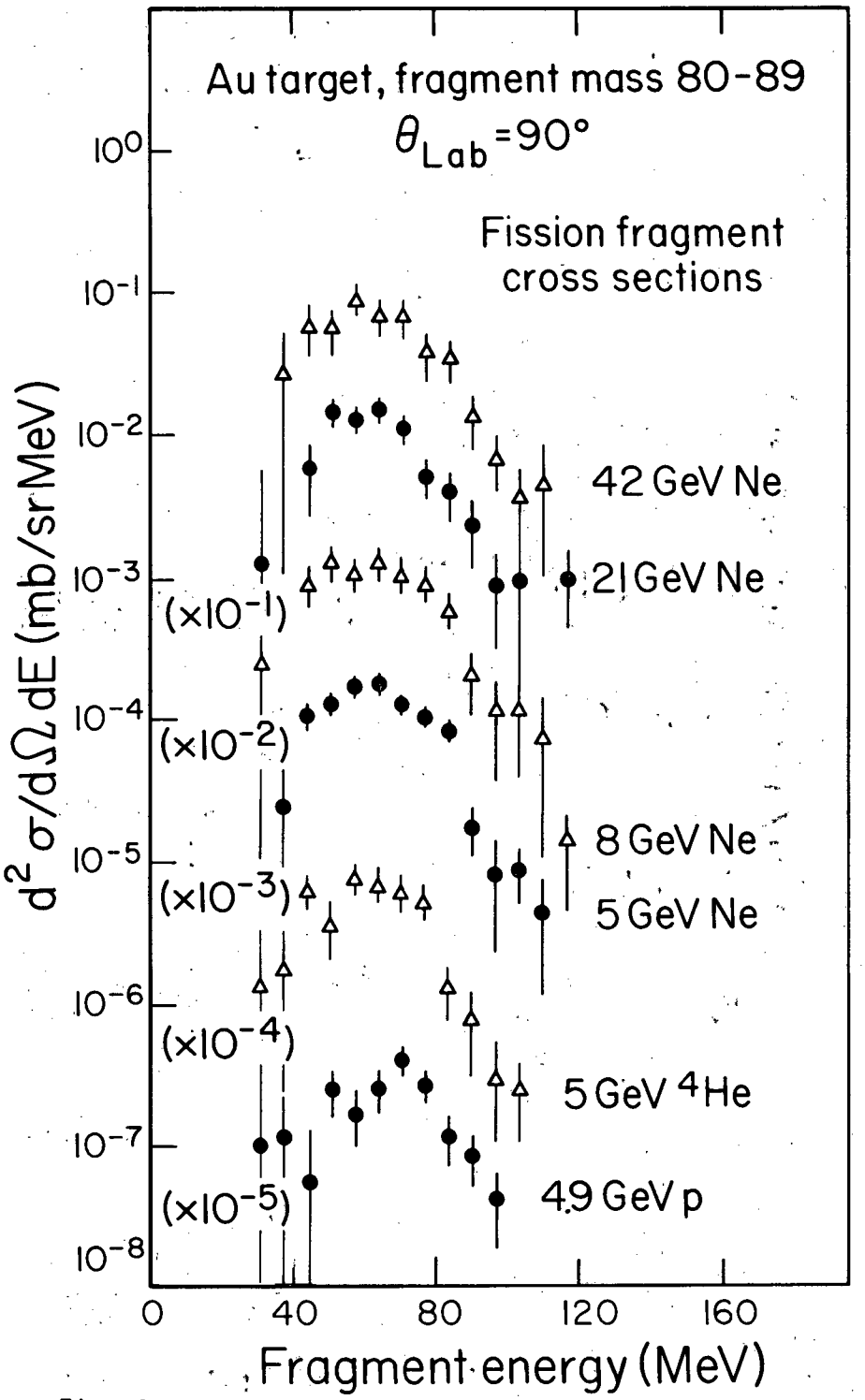

Fig. 6

XBL 823-244

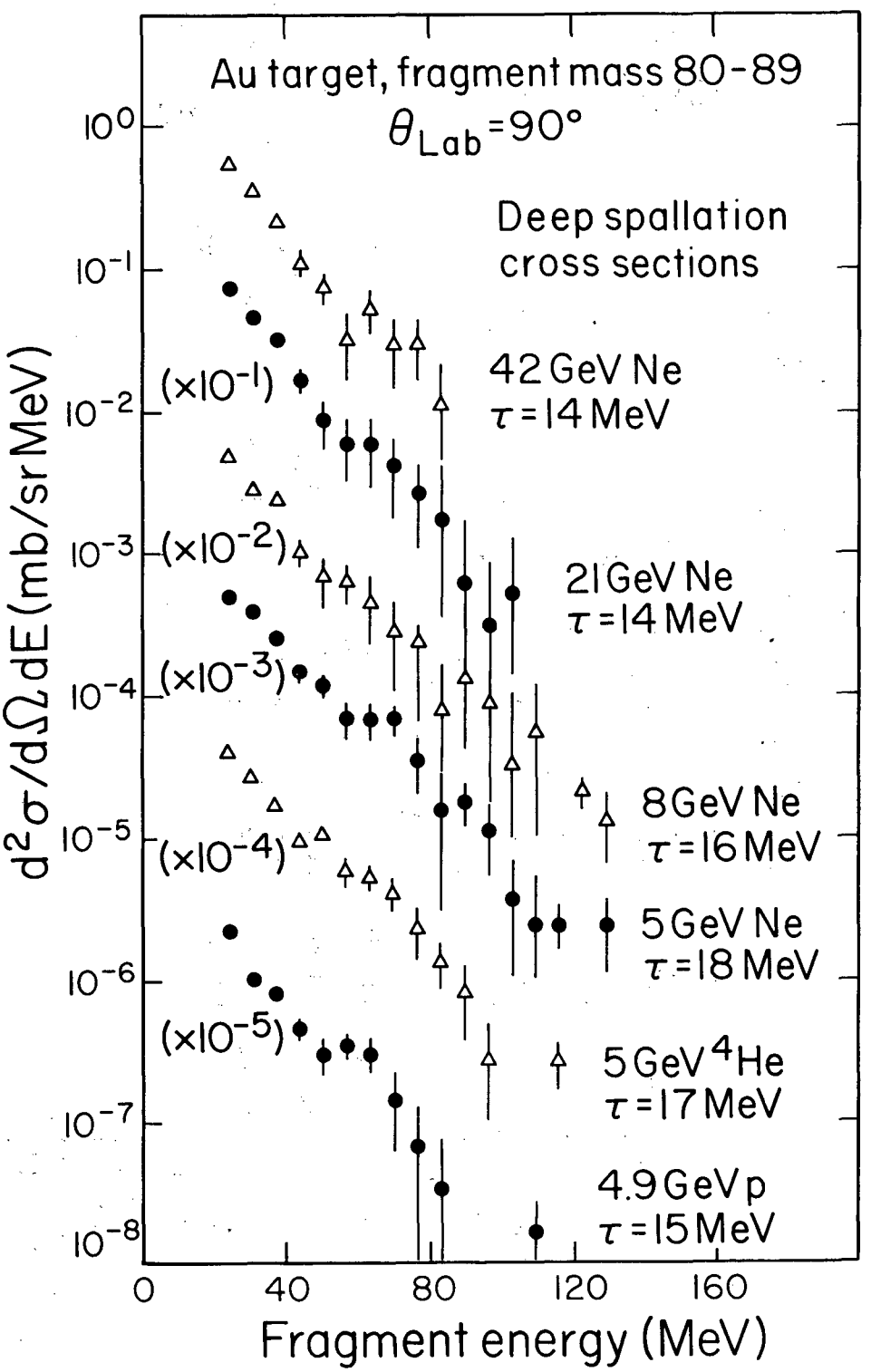

Fig. 7

XBL 8112-1650

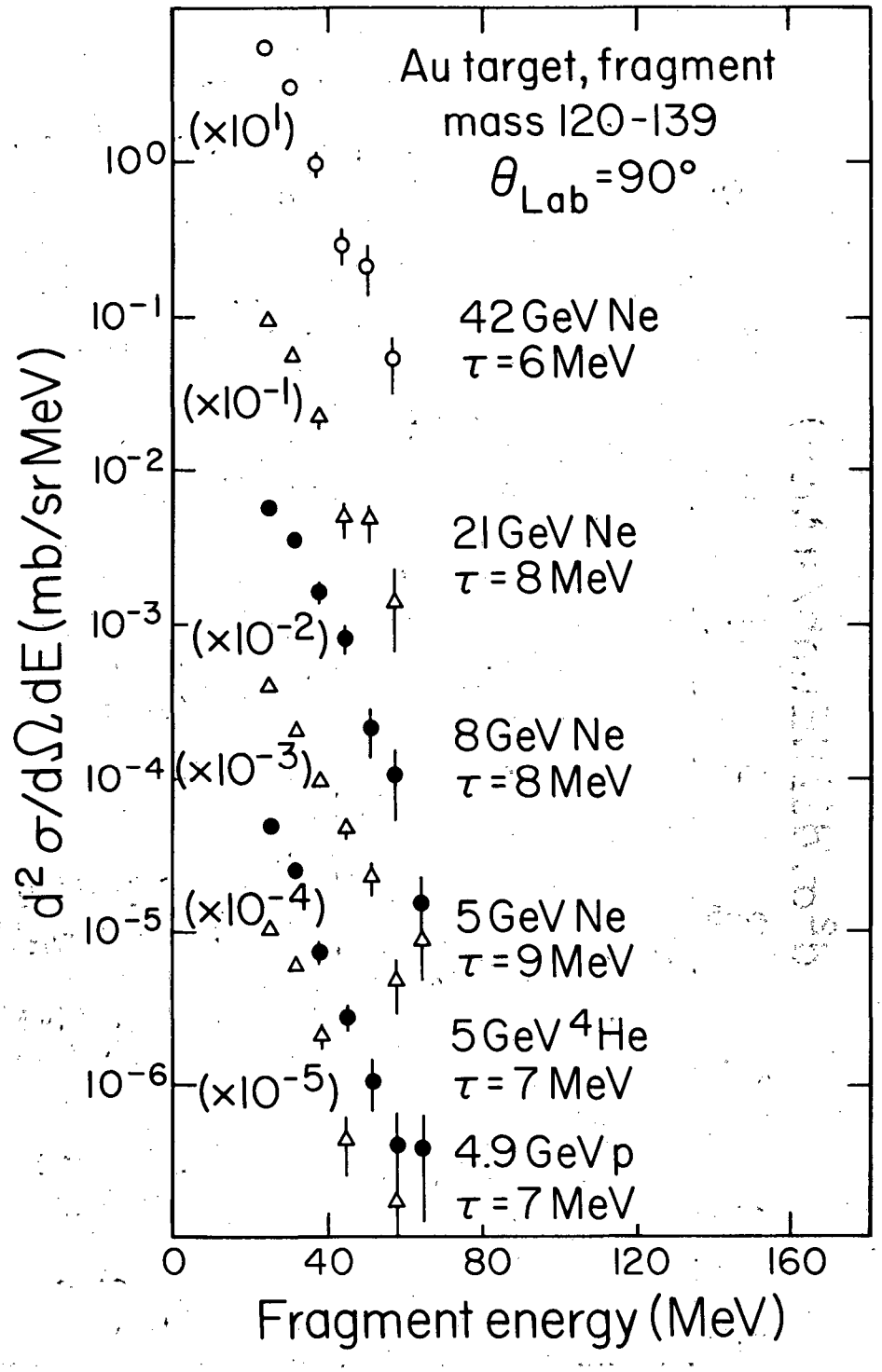

Fig. 8

XBL 8112-1651

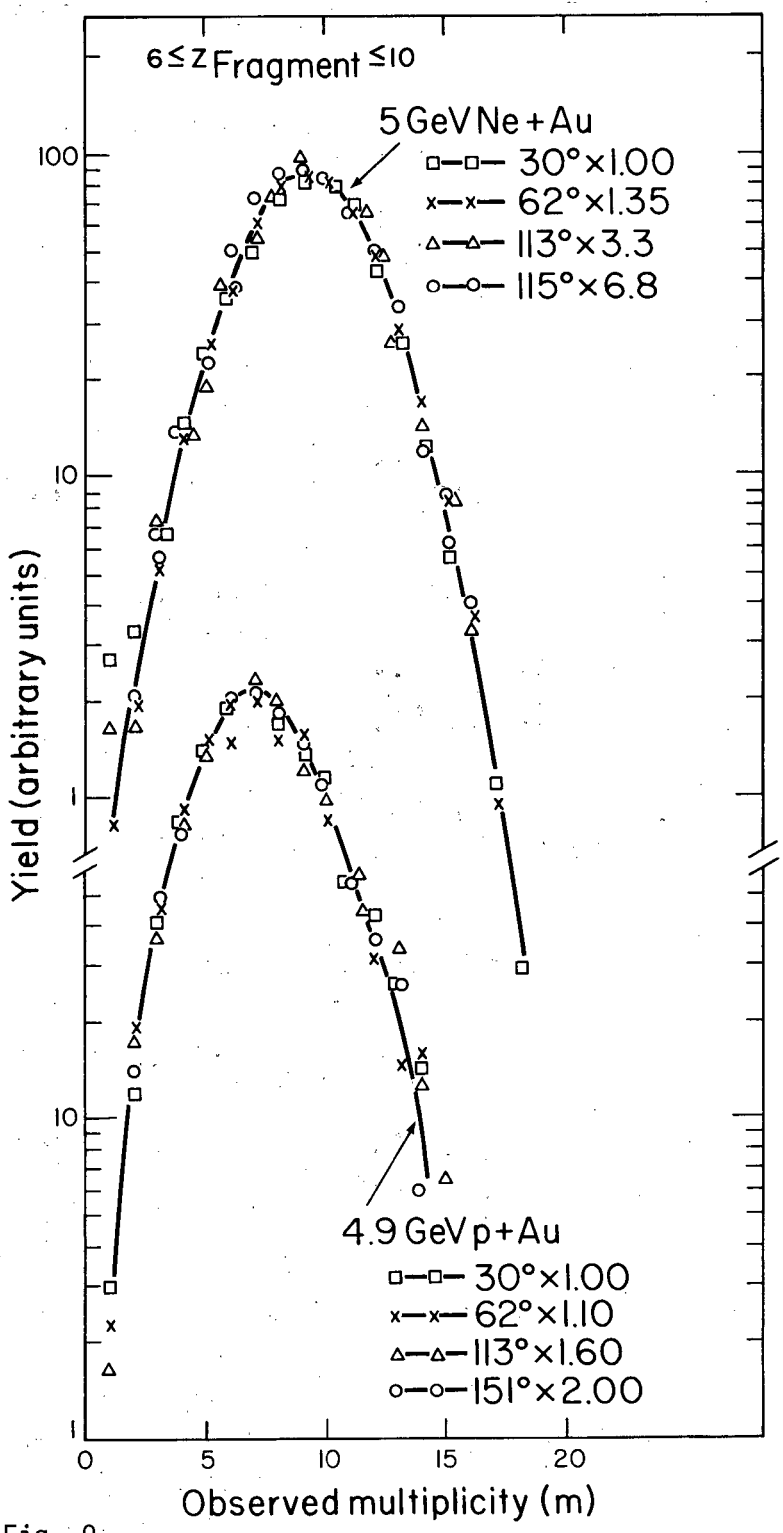

Fig. 9

XBL 8112-1656

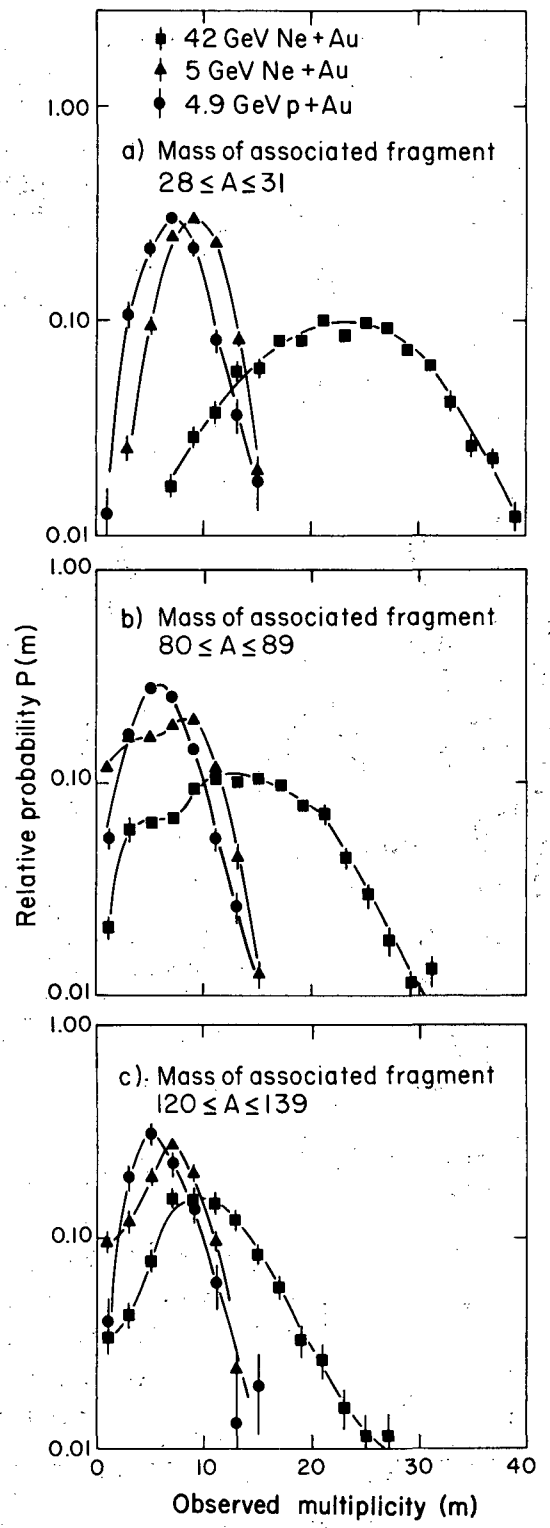

Fig. 10

XBL 827 – 894

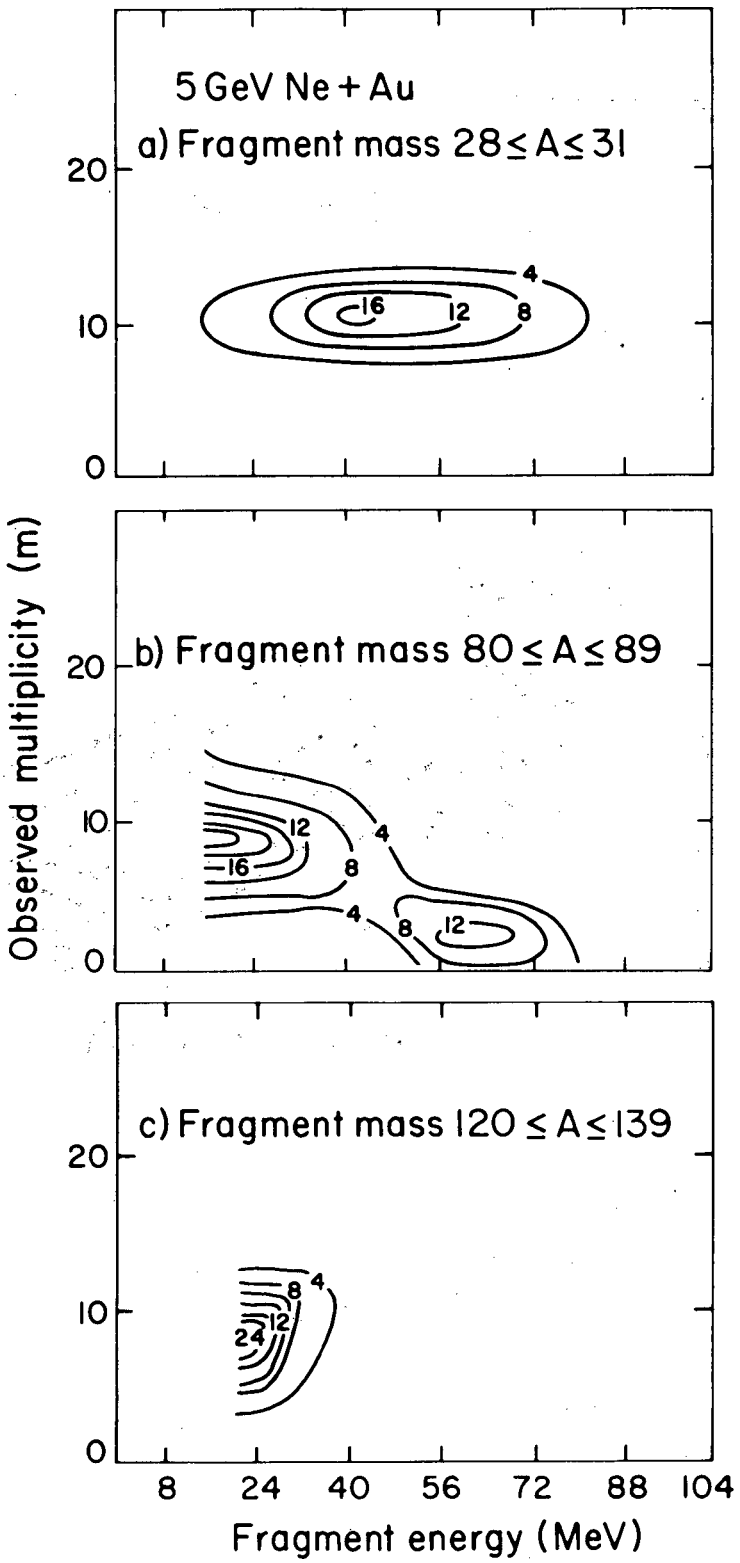

Fig. 11

XBL 827 – 892

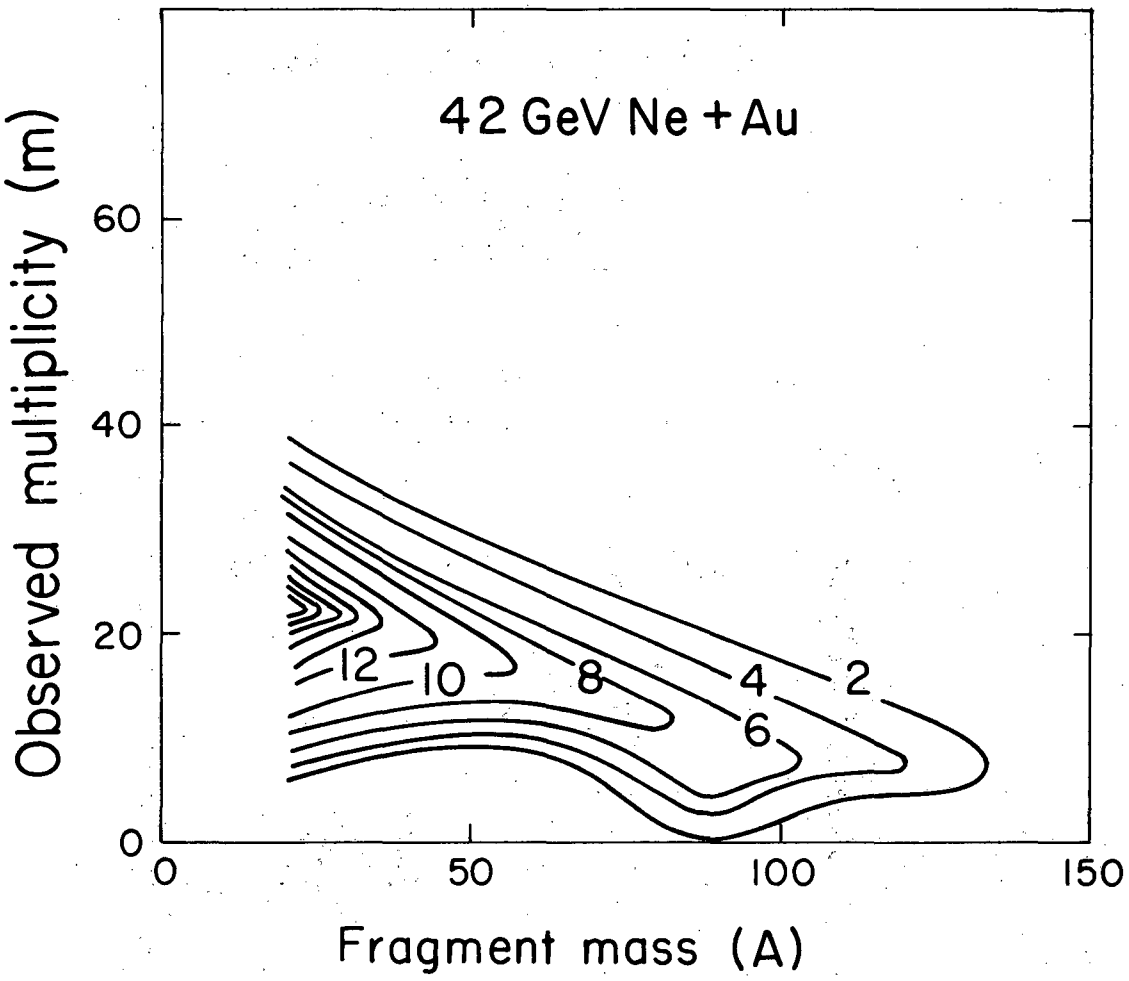

Fig. 12

XBL 824-409

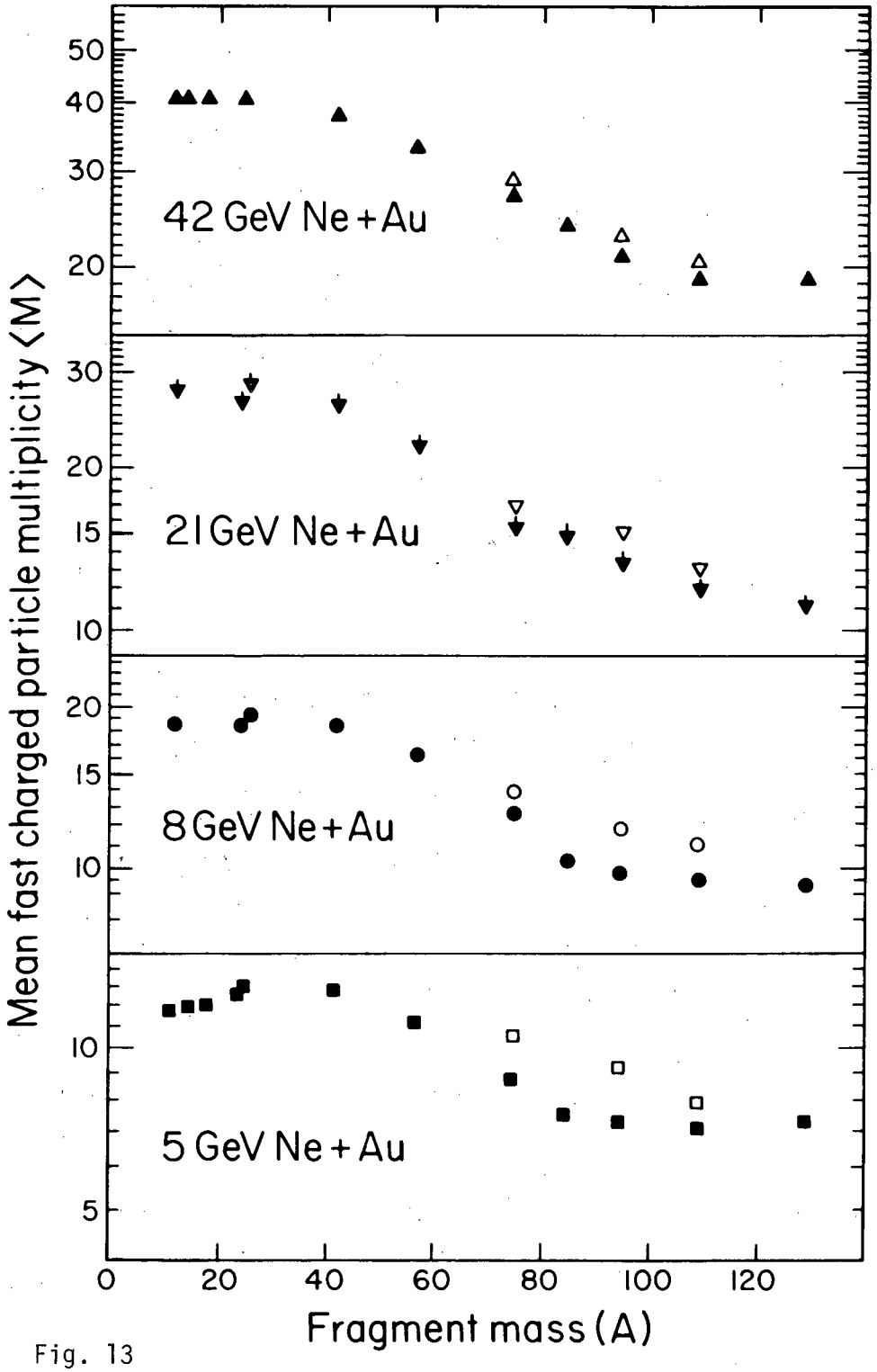

Fig. 13

XBL 827 – 891

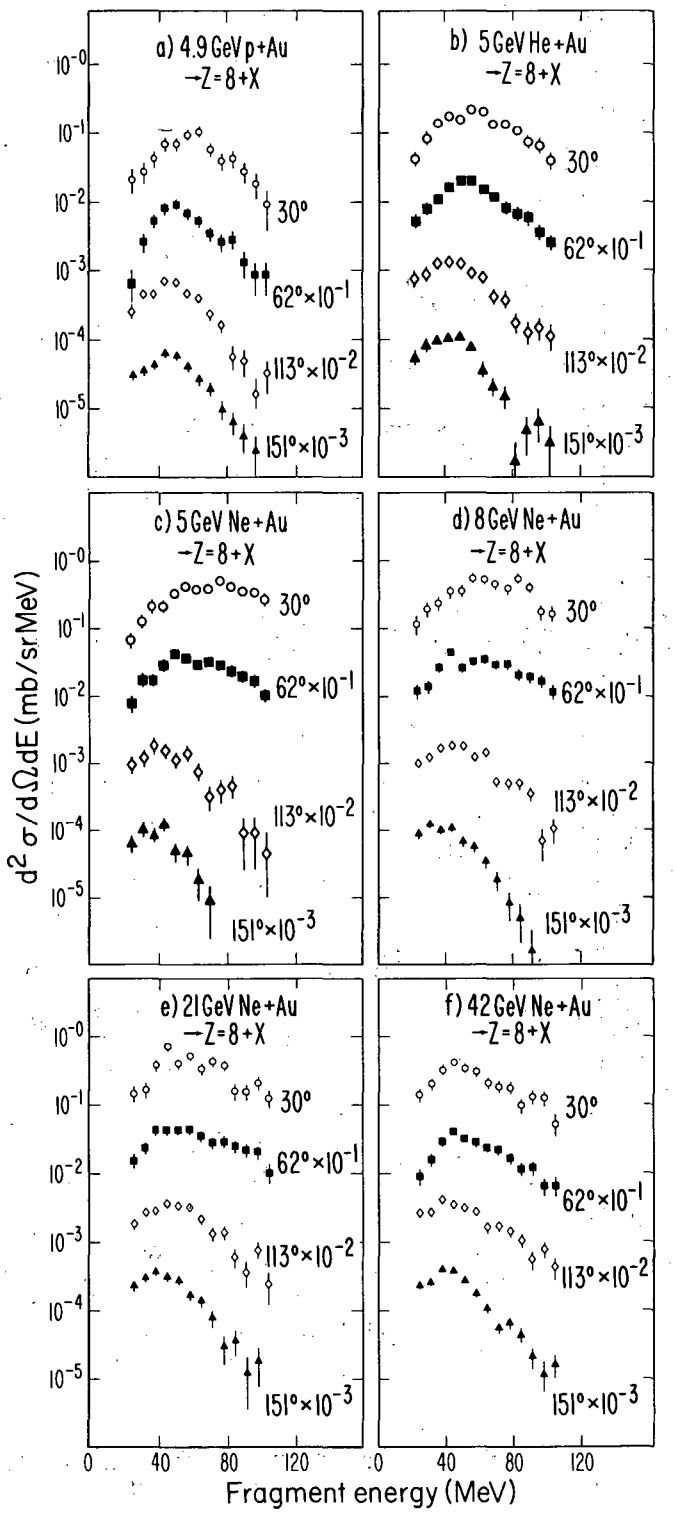
a) 4.9 GeV p+Au
→Z=8+X
b) 5 GeV He+Au
→Z=8+X
c) 5 GeV Ne+Au
→Z=8+X
d) 8 GeV Ne+Au
→Z=8+X
e) 21 GeV Ne+Au
→Z=8+X
f) 42 GeV Ne+Au
→Z=8+X
30°
62°×10⁻¹
113°×10⁻²
151°×10⁻³
d²σ/dΩdE (mb/srMeV)
Fragment energy (MeV)
0
40
80
120
XBL 827 – 895

Fig. 14

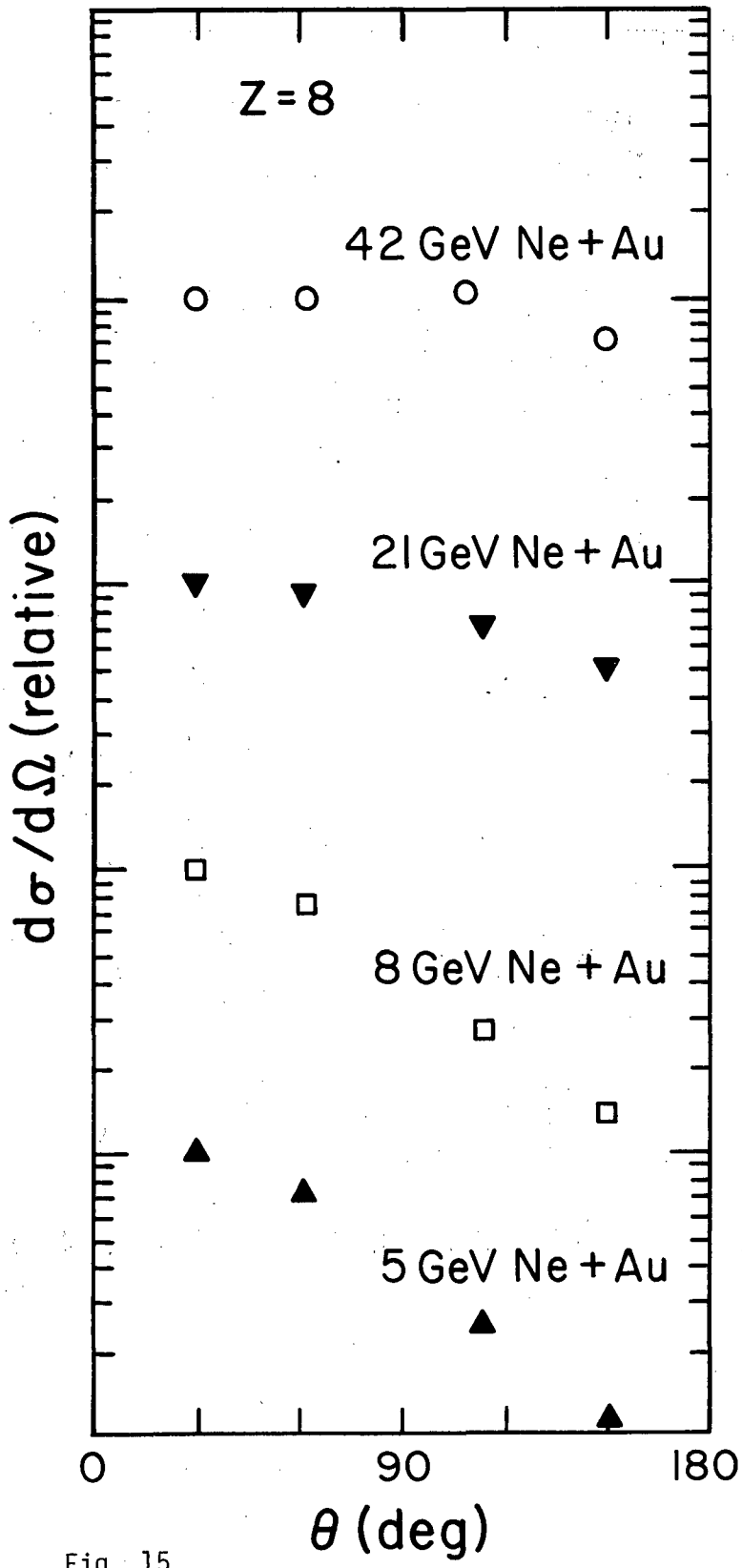

Fig. 15

XBL 827 – 890

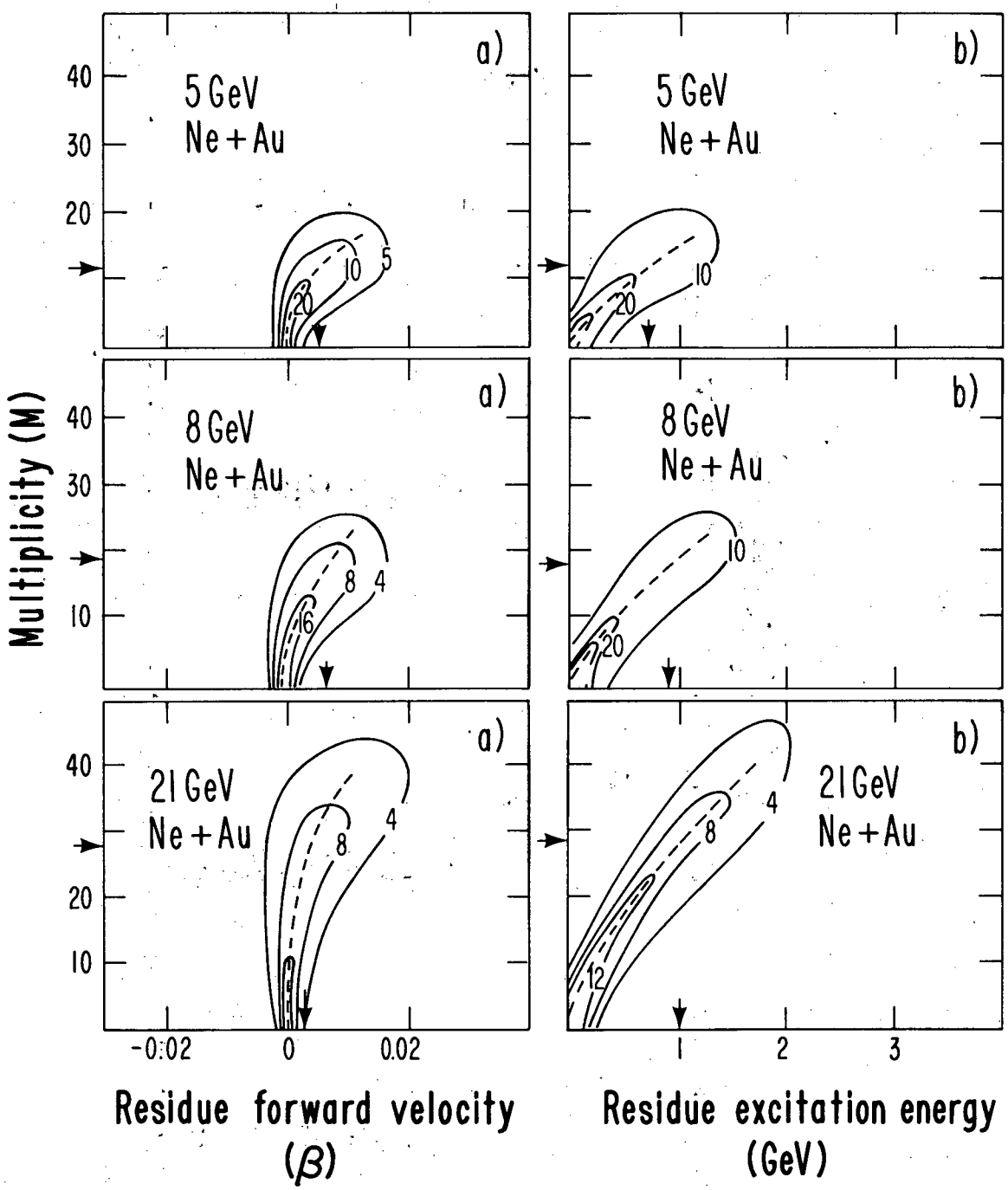

Fig. 16

XBL 824-410

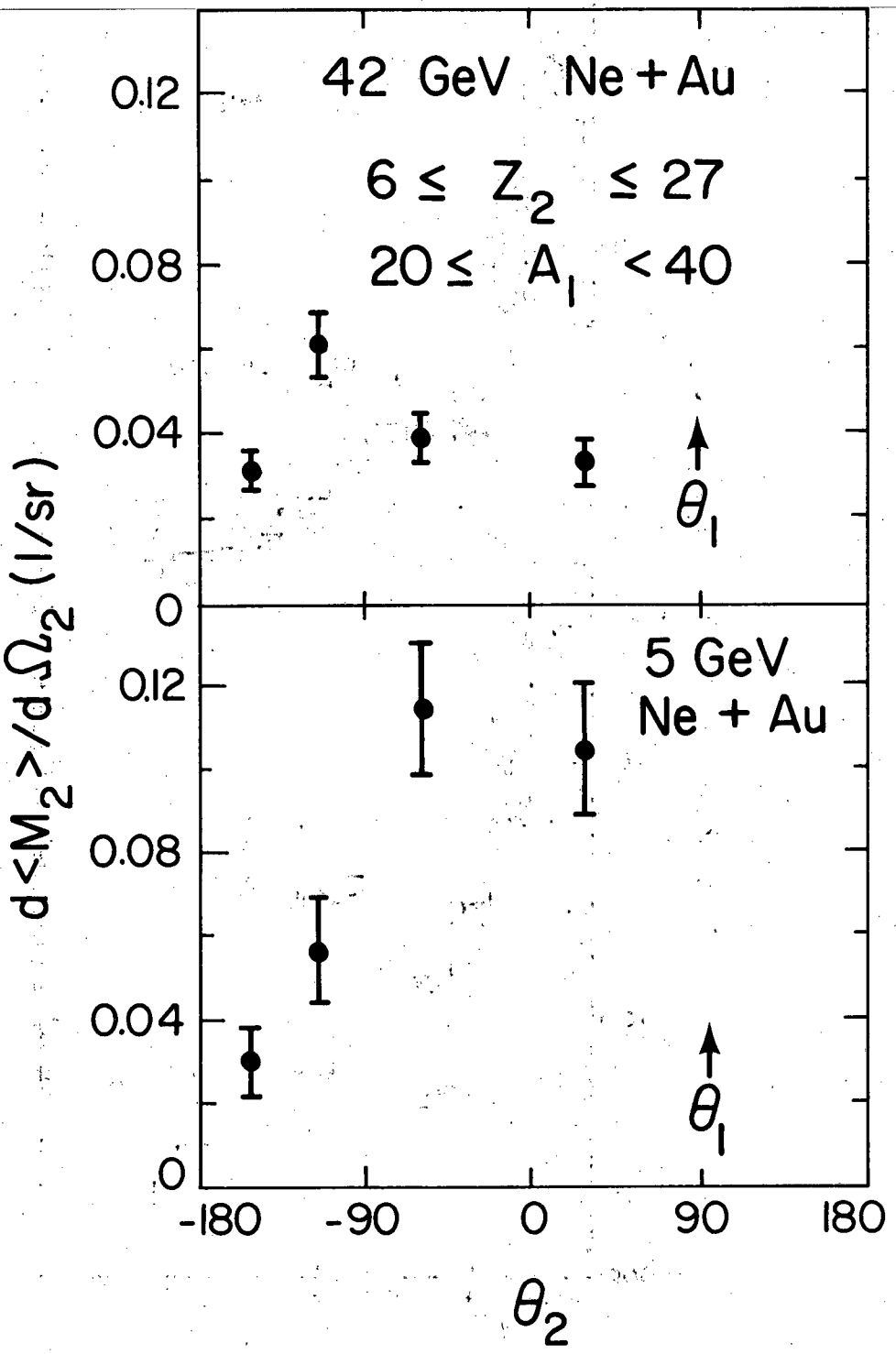

Fig. 17

XBL 821-43

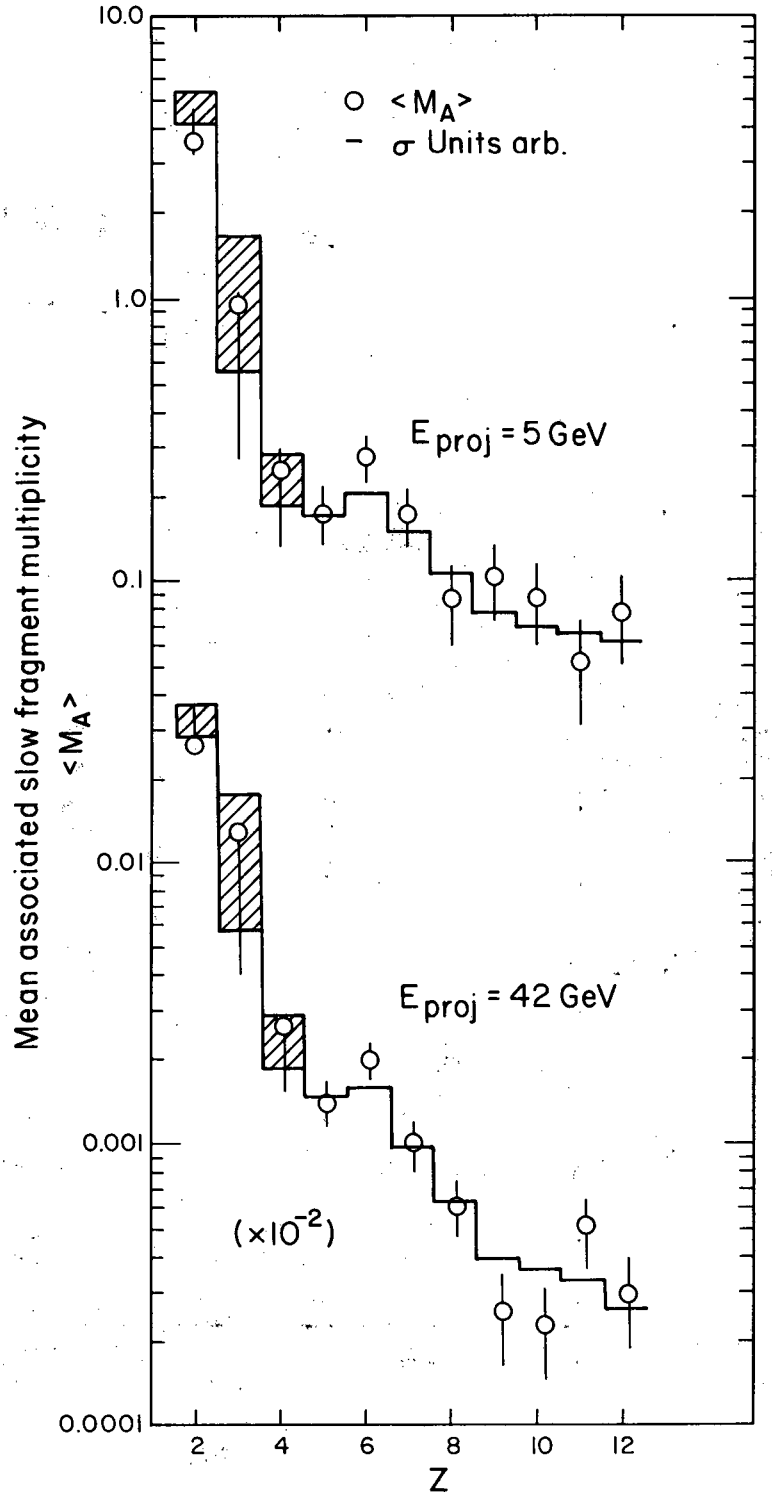

XBL 823-275

Fig. 18

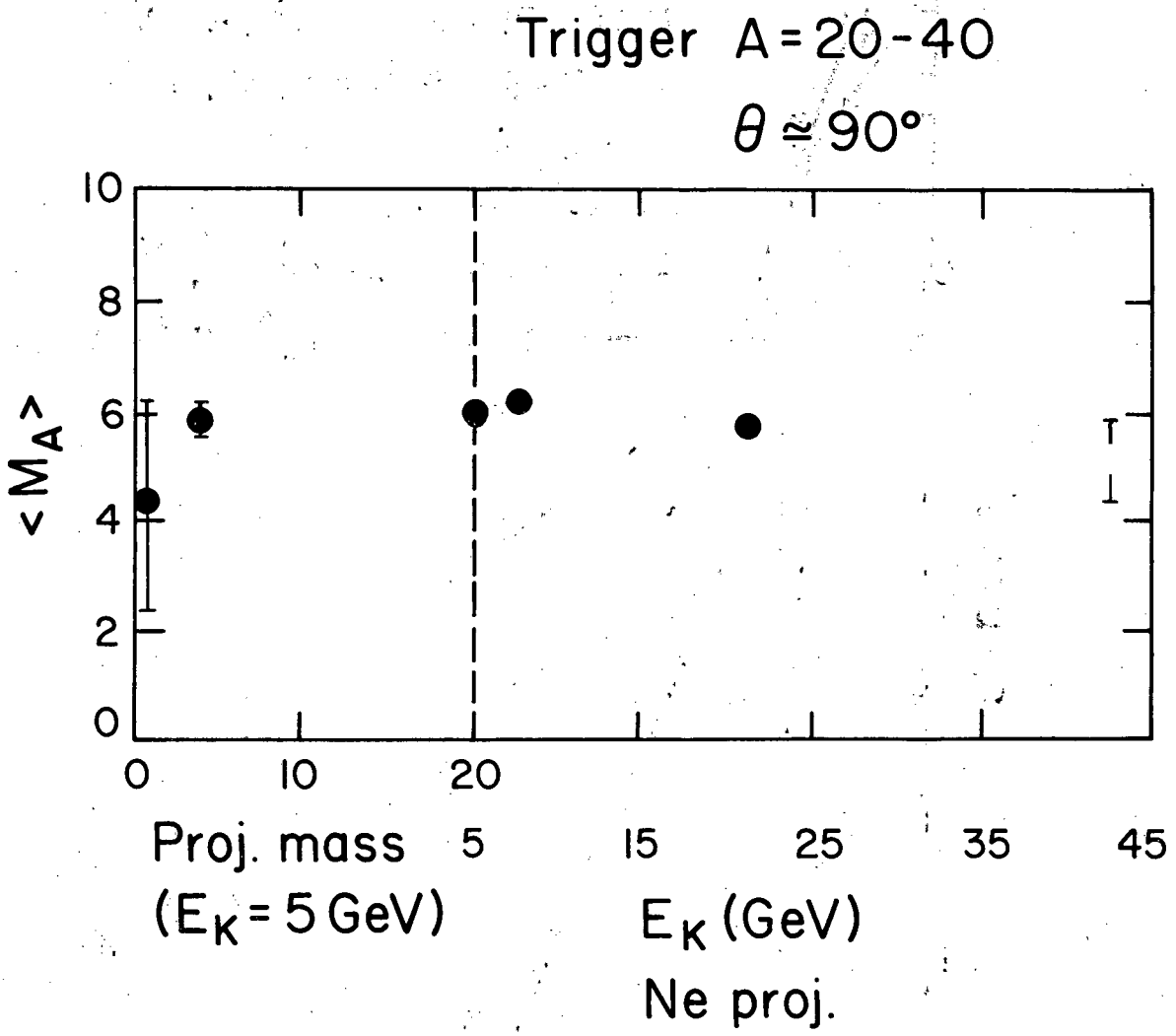

Fig. 19

XBL 823-276

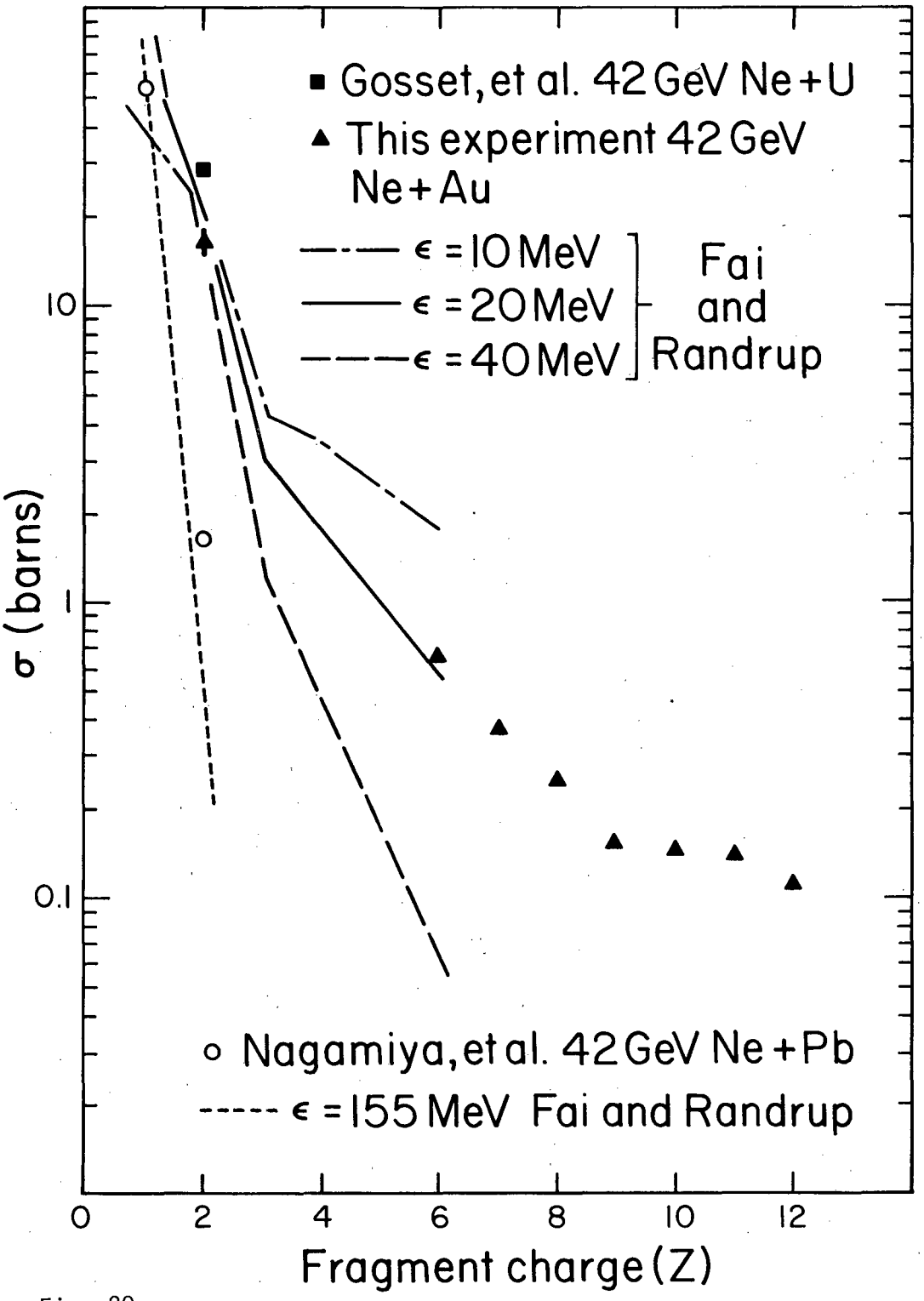

Fig. 20

XBL 827 – 889

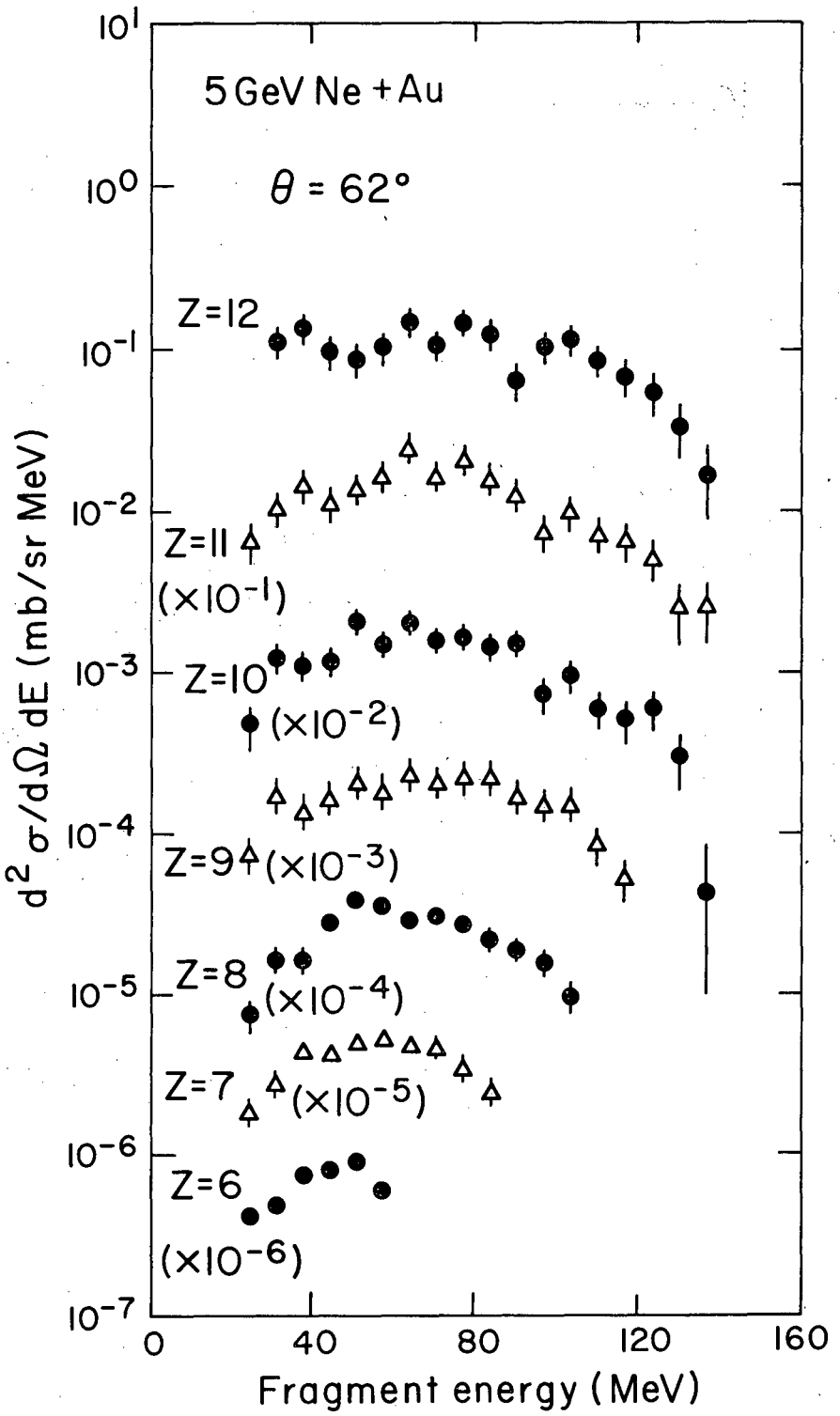

Fig. 21

XBL 822-138

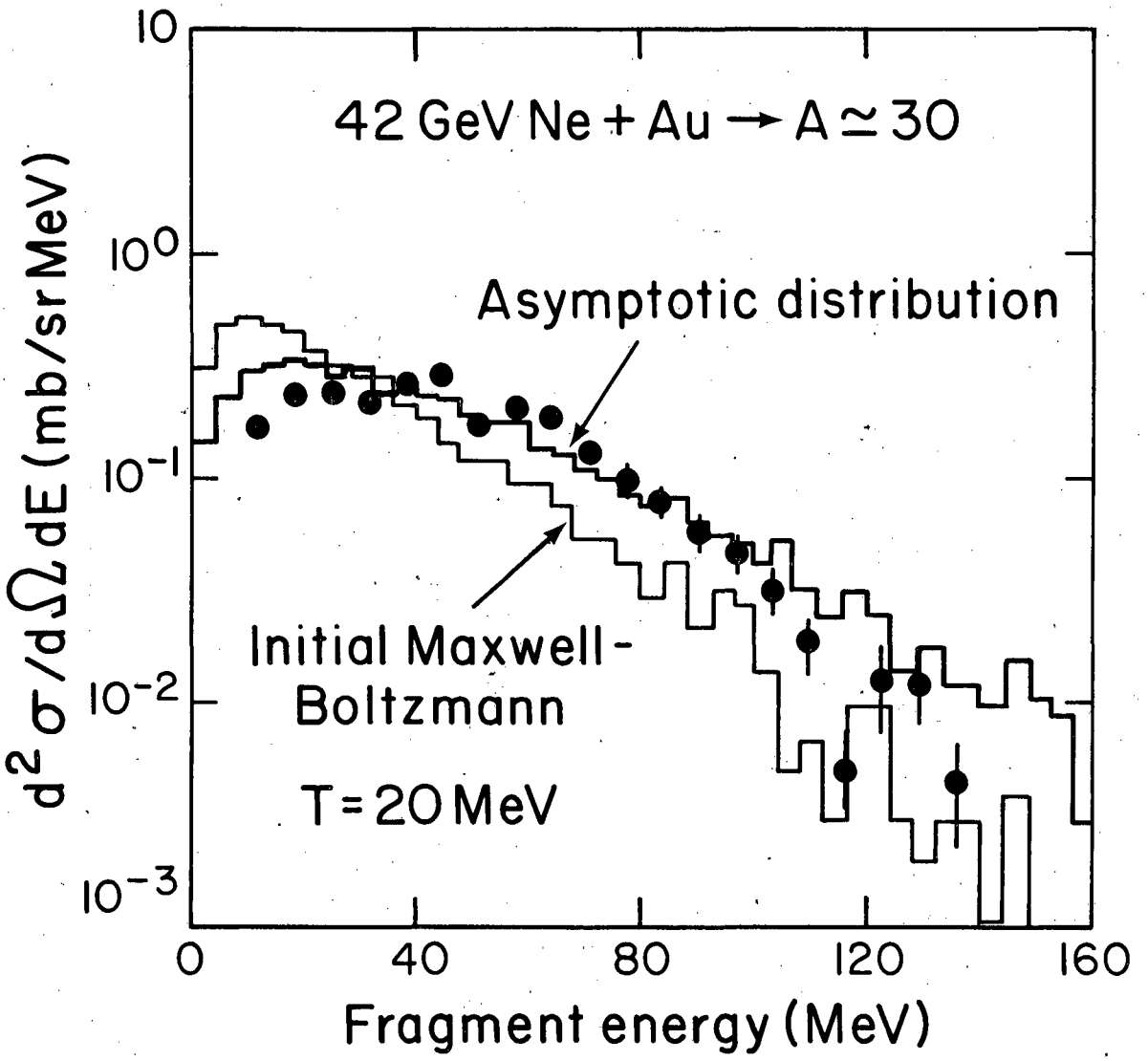

Fig. 22

XBL 827 – 940

TECHNICAL INFORMATION DEPARTMENT
LAWRENCE BERKELEY LABORATORY
UNIVERSITY OF CALIFORNIA
BERKELEY, CALIFORNIA 94720